NEW INSIGHTS INTO THE NATURE OF THE SMC WR/LBV BINARY HD 5980[1]

C. Foellmi,[2] G. Koenigsberger,[3] L. Georgiev,[4] O. Toledano,[3] S. V. Marchenko, [5] P. Massey,[6]
T. H. Dall, [7] A. F. J. Moffat,[8] N. Morrell,[9] M. Corcoran,[10,11] A. Kaufer,[12] Y. Nazé,[13]
J. Pittard,[14] N. St.-Louis,[8] A. Fullerton,[15] D. Massa,[16] and A. M. T. Pollock[17]

RESUMEN

Presentamos los resultados de una campaña de observaciones ópticas del sistema múltiple HD 5980, cuya estrella primaria sufrió una erupción importante en 1994. Atribuyendo la variabilidad de las líneas en emisión al movimiento orbital de las dos estrellas con un período de 19.3 días, deducimos sus masas. El comportamiento de las líneas fotosféricas indica que la fuente de "tercera luz" del sistema es probablemente también un sistema binario como fue propuesto por Schweickhardt (2000). Los datos presentados en este artículo estarán públicamente disponibles.

ABSTRACT

We present the results of optical wavelength observations of the unusual SMC eclipsing binary system HD 5980 obtained in 1999 and 2004–2005. Radial velocity curves for the erupting LBV/WR object (*star A*) and its close WR-like companion (*star B*) are obtained by deblending the variable emission-line profiles of NIV and NV lines. The derived masses $M_{\rm A} = 58 - 79\,M_\odot$ and $M_{\rm B} = 51 - 67\,M_\odot$, are more consistent with the the stars' location near the top of the HRD than previous estimates. The presence of a wind-wind interaction region is inferred from the orbital phase-dependent behavior of He I P Cygni absorption components. The emission-line intensities continued with the declining trend previously seen in UV spectra. The behavior of the photospheric absorption lines is consistent with the results of Schweickhardt (2000) who concludes that the third object in the combined spectrum, *star C*, is also a binary system with $P_{\rm starC} \sim 96.5$ days, $e=0.83$.

[1] Based on observations made with the NTT, MPI 2.2 m and Danish 1.5 m telescopes at ESO, La Silla, Chile.

[2] Laboratoire d'AstrOphysique de Grenoble, Saint-Martin d'Hères, France.

[3] Instituto de Ciencias Físicas, Universidad Nacional Autónoma de México, Cuernavaca, Morelos, Mexico.

[4] Instituto de Astronomía, Universidad Nacional Autónoma de México, Mexico.

[5] Department of Physics and Astronomy, Western Kentucky University, KY, USA.

[6] Lowell Observatory, AZ, USA.

[6] Gemini Observatory, HI, USA.

[8] Département de Physique, Université de Montréal, Quebec, Canada.

[9] Las Campanas Observatory, La Serena, Chile.

[10] CRESST and X-ray Astrophysics Laboratory NASA/ GSFC, MD, USA.

[11] Universities Space Research Association, MD, USA.

[12] European Southern Observatory, Santiago, Chile.

[13] FNRS and Institut d'Astrophysique et de Géophysique, Université de Liège, Belgium.

[14] School of Physics and Astronomy, University of Leeds,

Leeds, UK.

[15] Space Telescope Science Institute, MD, USA.

[16] NASA/GSFC, MD, USA.

[17] European Space Agency, European Space Astronomy Centre, Madrid, Spain.

1. INTRODUCTION

The Small Magellanic Cloud system HD 5980 consists of two very luminous components referred to as *star A* and *star B* in a relatively close, eclipsing and eccentric orbit and a third equally luminous source, referred to as *star C*, that may merely be a line-of-sight coincidence. The eclipsing nature of HD 5980 was discovered by Hoffmann, Stift, & Moffat (1978), although the actual 19.3-day orbital period was found by Breysacher & Perrier (1980; henceforth BP80), and more recently refined by Sterken & Breysacher (1997). The two eclipses were not separated equally in time, indicating an eccentric orbit

($e = 0.32$, Breysacher & Perrier 1991; $e = 0.27$ Moffat et al. 1998; $e = 0.30$ Kaufer et al. 2002). The presence of strong and broad emission lines as well as photospheric absorption lines led to its early classification as a WN+OB binary system (Azzopardi & Vigneau 1975; Walborn 1977; Breysacher & Westerlund 1978). However, Niemela (1988) showed that the Doppler shifts in the N IV 4057 and N V 4603 emission lines moved in anti-phase, concluding that *both* stars in the 19.3-day binary orbit were Wolf-Rayet stars of the nitrogen sequence (WN) and that the absorption-line spectrum had to arise in a third object. With this result, Niemela et al. (1997) estimated the masses of the two stars, $M_{\rm A} \sim 50\,M_\odot$ and $M_{\rm B} \sim 28\,M_\odot$. From the eclipse light curve, Breysacher & Perrier (1991, henceforth BP91) derived stellar radii, $R_{\rm A} \sim 21\,R_\odot$ and $R_{\rm B} \sim 15\,R_\odot$. Its location in the SMC implied a visual absolute magnitude $M_{\rm V}^{\rm sys} = -7.3$ mag (BP91) and the BP91 light curve analysis provided good constraints on the visual absolute magnitude for each of the three stars within the system, from which $M_{\rm V}^{\rm A} = -6.3$ mag, $M_{\rm V}^{\rm B} = -5.8$ mag, and $M_{\rm V}^{\rm C} = -6.1$ mag. These and other parameters for HD 5980 are summarized in the first column of Table 1, which contains information derived from data obtained prior to 1981. Results from data of other epochs is listed in Column 2 (1994; near the time of eruption) and in Column 3 (1999–2005; declining phase of the eruption).

The spectral characteristics and visual brightness of HD 5980 gradually changed between the late 1970's and 1993, when it entered an eruptive state that lasted ∼1 year (Bateson & Jones 1993; Barbá et al. 1995; Koenigsberger et al. 1995). The activity involved an increase in visual brightness and mass-loss rate, and a decrease in wind velocity and effective temperature, similar to the eruptive phenomena observed in LBVs. The radial velocity (RV) variations in the post-eruption emission-line spectrum led Barbá et al. (1996) and Barbá, Niemela, & Morrell (1997) to conclude that the instability producing the outbursts originated in *star A*. This was also confirmed by independent observations of Moffat et al. (1998). The hydrogen abundance in *star A* that was derived near the time of maximum eruption, when its emission-lines are believed to have completely dominated the combined spectrum, was found to be depleted (Koenigsberger et al. 1998b). Thus, *star A* is a very massive star that has left the Main Sequence. Another fascinating aspect of the system is that in the process leading up to the eruption, *star A* seems to have traversed the entire nitrogen-sequence (WN) of the WR classification system, starting out as a WN3 (Niemela 1988) and reaching WN11 (Drissen et al. 2001) during maximum eruption. This behavior is unprecedented.

It is important to note that the eruptive activity in HD 5980 has been recorded only once. Thus, *star A* may still be basically in the pre-LBV evolutionary phase, resembling one of the H-rich (or at least not yet H-poor), luminous WR stars of type WNh, or probably even WNha, like most, if not all, of the 10 other WN stars in the SMC (Foellmi, Moffat, & Guerrero 2003). These are not really *bona fide* WR stars in the classical sense, i.e. they are not in the He-burning stage.

Star B is also inferred to be a WR star based on pre-eruption spectroscopic observations that indicate emission-line RV variations consistent with this notion (Breysacher, Moffat, & Niemela 1982, henceforth BMN82). If both stars are, indeed, WR's, the time-variable wind of *star A* presents a unique opportunity for studying the effects that a changing wind momentum ratio produces on the wind-wind interaction (WWI). Curiously, however, the change in the WWI region during declining phases of the eruptive event appears to have had little effect on the observed X-ray emission (Nazé et al. 2007).

The masses of *star A* and *star B* are the central issue for establishing their evolutionary state. But a vexing problem arises when radial velocity curves of the emission lines are used to derive the stellar masses. The centroid of an emission line is ill-defined when the line is asymmetrical and undergoes strong variability over the orbital cycle, as is the case for HD 5980. Without a clear understanding of the line profile variations (lpvs), the orbital motion cannot be reliably ascertained and, hence, one cannot establish the primary cause of the variability.

The objectives of this paper are to use new and archival observations to establish constraints on the sources of the line-profile variability in HD 5980 and thus obtain RV curves that may be more representative of the orbital motion. § 2 summarizes the data; in § 3 we describe the line profile variability, leading to a new set of RV curves (§ 4) from which the masses of *star A* and *star B* are estimated; § 5 summarizes the evidence suggesting that the wind density of *star A* is diminishing over long timescales; § 6 describes the stationary photospheric absorptions; § 7 presents the results of the photometric monitoring; in § 8 we discuss the wind-wind interaction region; and in § 9 we present the conclusions.

2. OBSERVATIONAL DATA

The 2005/2006 observation campaign at ESO was coordinated by CF and GK. Spectroscopy was

TABLE 1

SUMMARY OF HD 5980 ESTIMATED PARAMETERS

Parameter	1979–1981	1994	1999–2005
P_{orb} (days)	19.2654	$\cdots$	$\cdots$
Orbital inclination (deg)	88[m]	$\cdots$	$\cdots$
a $(R_\odot)$	127[b]	$\cdots$	143–157[k]
e	0.3	$\cdots$	0.30±0.16 [k]
M_{A} $(M_\odot)$	50[b]	$\cdots$	58–79[k]
M_{B} $(M_\odot)$	28[b]	$\cdots$	51–67[k]
$M_{\mathrm{V}}^{\mathrm{sys}}$ (mag)	-7.3[a]	-8.7[e]	-7.6[h]
$M_{\mathrm{V}}^{\mathrm{A}}$ (mag)	-6.3	-8.6[e]	-6.5
$M_{\mathrm{V}}^{\mathrm{B}}$ (mag)	-5.8	$\cdots$	$\cdots$
$M_{\mathrm{V}}^{\mathrm{C}}$ (mag)	-6.1	$\cdots$	$\cdots$
R_{A} $(R_\odot)$	21[a]	> 160[d]	$\cdots$
	$\cdots$	280[g]	$\cdots$
R_{B} $(R_\odot)$	15[a]	$\cdots$	$\cdots$
R_{envB} $(R_\odot)$	30–40[a]	$\cdots$	$\cdots$
v_∞^{A} (km s^{-1})	$\cdots$	300–1700	1740–2200:
	$\cdots$	500[g]	$\cdots$
v_∞^{B} (km s^{-1})	3100:	$\cdots$	2600–3100:
v_∞^{C} (km s^{-1})	$\cdots$	$\cdots$	1700::
N[He]/N[H][aa]$_{\mathrm{Non-LTE}}$	$\cdots$	0.4[e]	$\cdots$
$\dot{M}_{\mathrm{A}}$ $(M_\odot$ yr$^{-1})$	$\cdots$	10^{-3}[e]	$\cdots$
$\dot{M}_{\mathrm{B}}$ $(M_\odot$ yr$^{-1})$	2×10^{-5}[m]		
L_{A} $(L_\odot)$	$\cdots$	3×10^6[e]	$\cdots$
	$\cdots$	10^7[g]	$\cdots$
T_*^{A} $^\circ$K	53,000[c]	21,000[d]	$\cdots$
	$\cdots$	35,500[e]	$\cdots$
Spectrum (Star A)	WN3[b]	$B1.5Ia^+$[d]	WN6[d]
Spectrum (Star B)	WN4[b]	WN4:	WN4:
Spectrum (Star C)	$\cdots$	$\cdots$	O4-6[f]
	$\cdots$	$\cdots$	O7I [n]
$V_{\mathrm{rot}}^{\mathrm{A}}$ sin i (km s^{-1})	$\cdots$	$\cdots$	250::[j]
$V_{\mathrm{rot}}^{\mathrm{C}}$ sin i (km s^{-1})	$\cdots$	$\cdots$	75[i]
P_{orb}(C) (days)	$\cdots$	$\cdots$	96.5[s]

[aa]Abundance ratio by number (0.63 by mass). [a]Breysacher & Perrier 1991. [b]Niemela et al. 1997. [c]Assuming L_{starA} $(L_\odot)$=const and $R_{\mathrm{starA}}/R_\odot$=21. [d]Koenigsberger et al. 1998a. [e]December 30, Koenigsberger et al. 1998b. [f]Koenigsberger et al. 2000. [g]Drissen et al. 2001. [h]S. Duffau, assuming m–M=19.1 mag. [i]Koenigsberger et al. 2001. [j]Georgiev & Koenigsberger 2004b. [k]This paper. [m]Moffat et al. 1998. [n]Koenigsberger et al. 2006. [s]Schweickhardt 2000.

obtained under service observing mode with the Fiber-Fed Extended Range Optical Spectrograph (FEROS) mounted on the MPI 2.2 m telescope at La Silla, and the ESO Multi Mode Instrument (EMMI) mounted on the NTT. In addition to these data, a set of archival FEROS observations obtained in 1999 on the 1.5 m telescopes at La Silla (Schweickhardt 2000; Kaufer et al. 2002) were retrieved. Photometric observations were obtained at Las Campanas in 2003, at ESO in 2005, and at CTIO in 2005–2006.

TABLE 2

FEROS 1999 DATA

Spectrum	MJD	Phase	NIV 4057.76			HI 4101.71			HeII 5411.52		
			RV km s^{-1}	FW km s^{-1}	−EW Å	RV km s^{-1}	FW km s^{-1}	−EW Å	RV km s^{-1}	FW km s^{-1}	−EW Å
78781	51374.418	0.475	13	685	3.83	76	1105	7.94	203	907	14.79
79411	51375.422	0.527	−10	694	4.46	63	1221	8.99	221	993	16.04
80871	51379.402	0.734	−50	689	2.99	56	1515	9.03	201	1217	15.62
81451	51380.398	0.786	−55	685	3.05	53	1546	8.80	211	1306	15.21
82121	51381.402	0.838	−23	705	2.79	47	1538	8.58	218	1249	14.84
83181	51382.352	0.887	−0.5	711	3.03	66	1505	8.91	227	1213	15.18
83811	51383.355	0.939	50	679	3.14	97	1527	9.08	251	1188	14.11
84511	51384.309	0.989	116	697	3.39	113	1316	8.51	226	1066	13.48
85181	51385.332	0.042	197	663	3.72	187	1072	9.41:	317	769	13.27
85771	51386.391	0.097	229	760	3.46	210	1297	8.55	340	1023	14.22
86321	51388.340	0.198	187	810	3.98	233	1553	8.54	404	1185	12.99
86701	51389.383	0.252	138	752	3.53	230	1424	8.02	399	1049	13.06
87211	51390.328	0.301	118	647	3.46	143	1373	8.41	328	1070	14.01
87751	51391.332	0.353	92	624	2.68	66	1215	7.42	207	946	13.46
88931	51392.328	0.405	49	609	3.28	43	1170	8.48	175	872	15.55
89511	51393.371	0.459	23	658	3.57	55	1118	8.22	195	880	14.91
90131	51394.391	0.512	0.5	671	3.76	54	1136	8.43	210	921	15.82

2.1. Spectroscopy

The 33 FEROS echelle spectra reported in this paper were obtained with a 2 k × 4 k EEV CCD, and they cover the whole optical range (∼3750–9200 Å). The spectral resolving power of FEROS is 48000. Typical exposure times for the 1999 data were between 40 and 50 minutes, while those of the 2005 data were typically 27 minutes. The S/N∼30–70 per resolution element in the collapsed 1D spectrum, lower values corresponding to the blue spectral region. Tables 2 and 3 contain the ephemerides of these observations.

The "pipeline" FEROS data reduction was checked by LG against sample detailed processing using MIDAS and IDL routines and was found to provide similar results, and thus we chose to use the "pipeline" reduced spectra. Data analysis was performed by GK. The merged spectrum in the wavelength range 3900–8500 Å was normalized in a three-step process. In the first step, all the spectra were combined for each epoch (1999 and 2005, respectively) so as to automatically remove cosmic rays. In the second step, the continuum was traced using a linear interpolation between small wavelength intervals over which the location of the continuum could be relatively well established. This yielded a

curve that approximately describes the shape of the continuum on the average spectrum and that was then used to rectify the continuum on each of the individual spectra. After the spectra were normalized in this manner, the third step consisted in fitting a spline function ("spline3" in IRAF) of order 3, 6 or 15 to arrive at the normalized spectrum for the whole wavelength range stated above. However, for the detailed comparison of the line profiles and RV measurements, selected spectral windows were extracted from the whole normalized spectrum, and renormalized individually by fitting a second order Legendre function to the neighboring continuum levels. Cosmic rays in spectral windows to be measured were removed individually, and a Gaussian smoothing procedure was applied to enhance the S/N ratio per wavelength interval.

Spectra obtained near mid-continuum eclipses need to be renormalized so that the comparison of line profiles is meaningful. Because the orbit is eccentric, eclipses are not equidistant in phase; they occur at $\phi=0$ (star A "in front") and at $\phi=0.36$ (star B "in front"). From the BP91 light curve solution, the $\phi=0$ eclipse is total while at $\phi=0.36$, only ∼50% of star A's continuum is occulted. The relative continuum levels for stars A, B and C are, respec-

TABLE 3

FEROS 2005 DATA

Spectrum	MJD	Phase	NIV 4057.76			HI 4101.71			HeII 5411.52		
			RV km s^{-1}	FW km s^{-1}	−EW Å	RV km s^{-1}	FW km s^{-1}	−EW Å	RV km s^{-1}	FW km s^{-1}	−EW Å
0617801	53538.385	0.799	−29	760	2.56	21	1860	5.82	211	1622	15.33
0617531	53538.404	0.800	−31	756	2.63	12	1903	5.80	221	1643	14.56
0620221	53541.384	0.955	78	800	2.70	136	1692	5.31	278	1454	12.96
0620344	53541.403	0.955	73	810	2.99	120	1608	5.62	291	1497	13.38
0710740	53561.367	0.992	98	745	3.13	141	1409	6.37	281	1099	14.07
0710950	53561.386	0.993	98	729	3.11	143	1395	5.98	284	1068	14.83
0725580	53576.288	0.767	−10	817	2.65	91	2003	5.13	270	1705	15.39
0725630	53576.307	0.767	−3	828	2.76	77	1921	5.82	266	1654	15.03
0921331	53635.000	0.814	−19	936	2.32:	23	1952	4.62	216	1747	15.36
0922990	53635.019	0.815	−2	955	2.36	56	2026	5.57	202	1757	14.99
0925220	53638.253	0.983	118	694	2.75	174	1452	5.11	295	1239	13.38
0925481	53638.272	0.984	113	758	2.54	178	1427	4.97	285	1192	13.24
0928220	53641.153	0.133	249	986	2.46	?	?	4.60	420	1629	13.50
0928161	53641.173	0.134	260	921	2.40	?	?	4.82	420	1627	13.46
1022700	53665.026	0.372	85	657	2.53	16	1290	5.72	159	1088	15.75
1022731	53665.045	0.374	86	666	2.53	21	1288	5.59	153	1048	15.92

tively, I_A=0.41, I_B=0.26 and I_C=0.33. Hence, to correct for the continuum eclipses, we added I_B at ϕ=0.00 and $0.7I_A$ at ϕ=0.36–0.37 (see below), and then renormalized the continuum to unity. It must be emphasized that this renormalization is only a gross approximation, since no recent (i.e., for data taken after 1980) light curve solution is available to provide current values of the stellar radii. However, under the assumption that only *star A* changed its size, it is pretty certain that the eclipse at ϕ=0 is a total eclipse. In addition, FUSE observations lead to the conclusion that the ratio of the radii of *star A* and *star B* in 2002 was similar to that obtained by BP91. This would suggest that the correction at this phase be only $0.5I_A$. However, this correction leads to an increase in the line-to-continuum ratio at eclipse, contrary to what is expected, especially since a fraction of *star A*'s line emission must be eclipsed, leading to the conclusion that a larger correction is required. This leads to the correction value of $0.7I_A$ given above. Such a larger correction is justified when limb-darkening is taken into account.

The ESO Multi Mode Instrument (EMMI) was used in the red mode (RILD) with the low-resolution grism 2, leading to a resolution of 300–1700 in the wavelength range 4000–10000 Å. Typical exposures were 20s for HD 5980. EMMI data were processed

TABLE 4

EMMI DATA

Spectrum	MJD	Phase
0619	53541.389	0.955
0630	53552.429	0.528
0710	53561.400	0.994
0921	53634.999	0.814
0924	53638.238	0.982
0927	53641.176	0.135
1010	53654.110	0.806
1012	53656.164	0.913

by OT using standard IRAF routines. This processing consists of cosmic ray excision, bias subtraction, flat-field correction, wavelength calibration, background sky subtraction and extraction to produce a one-dimensional spectrum. Background includes the strong ISM lines that are produced by the large H II region N66 within which HD 5980 is located. Three spectra were obtained on each night, and these were averaged together and normalized using an interactive polynomial fit to line-free continuum regions. Wavelength calibration was done with the HeAr lamp exposures obtained on the same nights as

TABLE 5

AVERAGE DIFFERENTIAL PHOTOMETRY: DANISH TELESCOPE

<MJD>	<Phase>	Num.	$< m_v - C >$	$< \sigma_{\mathrm{instr}} >$	s.d.
53561.422	0.995	20	-1.244	0.008	0.014
53562.352	0.043	18	-1.397	0.007	0.008
53564.352	0.147	12	-1.501	0.008	0.006
53568.305	0.352	7	-1.234	0.006	0.003
53576.367	0.771	43	-1.423	0.008	0.006
53684.203	0.368	172	-1.186	0.004	0.013
53685.105	0.415	30	-1.375	0.003	0.004
53687.207	0.524	41	-1.440	0.005	0.007
53689.191	0.627	95	-1.442	0.006	0.006
53693.184	0.834	20	-1.452	0.006	0.007
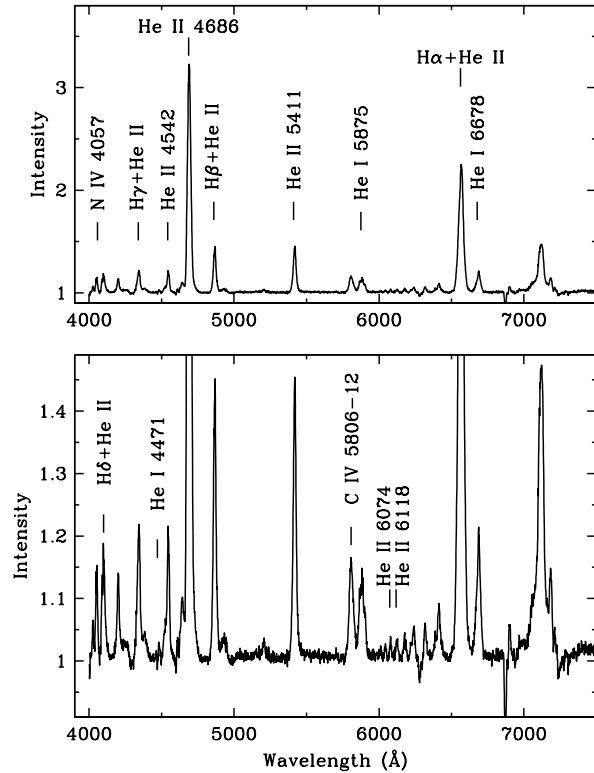
Fig. 1. Average $\phi \sim 0$ low dispersion spectrum obtained with EMMI in 2005 and rectified. The strongest line in the spectrum is He II 4686 Å. Other lines mentioned in the text are labeled with their primary identifications. The same spectrum is amplified in the lower panel, to display more clearly the weaker lines.

the exposures of HD 5980. Table 4 contains a summary of the EMMI data, and Figure 1 illustrates the 4000–7500 Å region of the average EMMI spectrum at orbital phase 0.00. Prominent emission lines are identified.

2.2. *Photometry*

Observations with the Danish 1.5 m telescope, using DFOSC and the V Johnson filter, were coordinated by TD and obtained over the time period JD 2453561–2453693. DFOSC is a focal reducer imager and spectrograph, covering a $13' \times 13'$ field of view. Data processing was carried out by SM as follows. The available CCD images were reduced with standard IRAF procedures. Following the general approach of Everett & Howell (2001), a weighted combination of fluxes of multiple comparison stars was introduced in order to produce differential magnitude values, $< m_v - C >$. This approach provides a typical accuracy σ_{instr}=0.003–0.008 mag for each individual observation, as listed in Column 5 of Table 5. In Table 5, Columns 1–3 list the average MJD of the observations, the orbital phase, and the number of differential magnitude determinations that were averaged to yield the $< m_v - C >$ listed in Column 5. The standard deviation, s.d., for this average is listed in Column 6.

In addition to the above, we include V-band observations obtained by NM from JD 2452975.56 to 2452991.57 on the 1 m Swope Telescope, at Las Campanas Observatory, and data that were taken from JD 2453591.88 through 2454092.70 for PM by the SMARTS consortium on the CTIO/SMARTS 1.0 m telescope. Both sets were processed by PM and converted to the visual magnitude scale. Part of the SMARTS data overlap in time with the Danish Telescope photometry, filling in the gaps in orbital phase not covered by the latter. The photometry of the Swope and SMARTS data was done relative to other

stars in the NGC 346 cluster, with the zero-point set by comparison of the data from a single (arbitrary) exposure to the photometry of Massey, Parker, & Garmany (1989). Within each data set, the photometry has a relative accuracy of ∼0.02 mag.

3. LINE PROFILE VARIABILITY

Line-profile variability in WR binaries is a major obstacle for determining the stellar masses. This is because the amplitudes of the RV curves obtained from variable and asymmetric line profiles depend on the way in which the lines are measured. In HD 5980, emission line-profile variability has been a common feature since the star was first observed spectroscopically (Breysacher & Westerlund 1978). Remarkably, the nature of the variability has remained qualitatively the same over many years, despite the strong changes that have occurred in the stellar wind properties. For instance, emission lines are always broader near elongations, while near eclipses they are visibly narrower and more sharply peaked (BMN82; Moffat et al. 1998), as illustrated by the Balmer-series lines of hydrogen that are plotted in Figure 2. The left panels of Figure 2 correspond to eclipse phases and those on the right to orbital phases near elongations. Most of the emission lines display the same pattern of variability.

The change in full-width at half maximum (FWHM) is illustrated in Figure 3 obtained from the Gaussian function fits to HI (+He II) 4101, N IV 4057, He II 5411, and CIV 5806/12 Å as a function of orbital phase, showing that different lines behave differently. However, the qualitative nature of the variations we observed in 1999 was as reported in previous optical observations (Moffat et al. 1998; BMN82; Breysacher & François 2000). This effect is only one aspect of a much more complex phase-dependent line profile variability pattern that involves asymmetric distortions of the line shape. Thus, the amplitude of any RV curve derived from the emission lines depends on how the lines are measured; that is, it depends on where within the system the emission lines are assumed to originate.

Fortunately, optical and UV spectroscopic monitoring of HD 5980 since the late 1970's provides the first of three pieces of solid information to aid in interpreting the variability: numerous emission lines that are currently present in the spectrum were absent prior to the early 1980's. The RV variations of the "new" lines indicate that they arise in *star A*. This is also true of the "new" UV lines observed with IUE and HST (Koenigsberger 2004 and references therein).
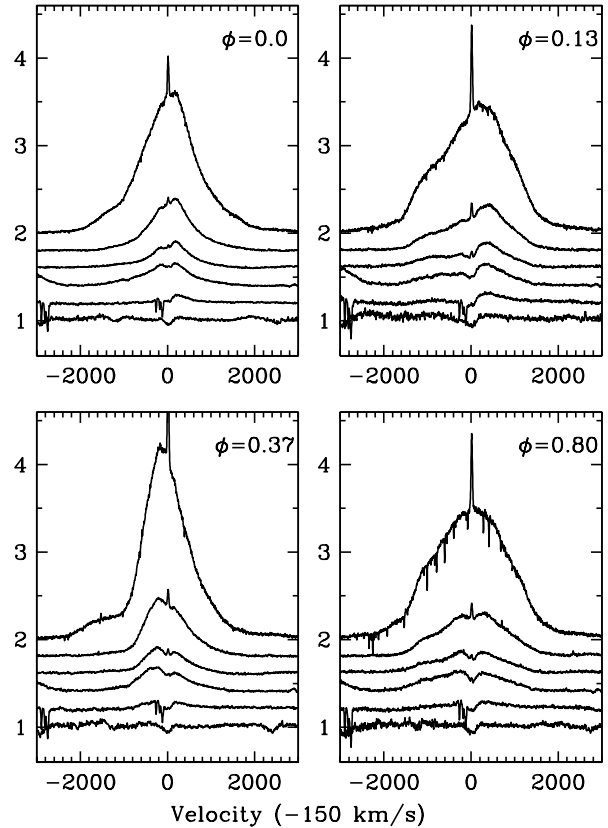

Fig. 2. H I (+He II) line profiles at Hα, Hβ, Hγ, Hδ, Hε and H9 3835 Å from FEROS 2005 data. The spectra are averages for each of the orbital phases ϕ=0.0, 0.13, 0.37 and 0.80; the spectra at ϕ=0.0 and 0.37 are renormalized to account for the corresponding eclipses. The velocity scale is corrected for the +150 km s^{-1} systemic velocity of the SMC. Sharp emission spikes, strongest at Hα, are nebular emission.

A second fact is that lines arising primarily in the inner portions of the stellar wind are less susceptible to distortions due to wind-wind interaction effects than lines that arise from outer wind regions. The former tend to originate from atomic transitions between excited states and from elements of lower chemical abundance, and are visible only because the density of the inner, accelerating portions of the wind is sufficiently large. Hence, lines from abundant ions and having large transition probabilities, such as Hα +He II 6560 Å and He II 4686 Å should be avoided during the RV curve analyses, while lines such as N IV 4057 Å may better describe the orbital motion.

The third datum that aids in the interpretation of the lpv's is that the system is eclipsing and the largest RV's occur near orbital phase ϕ=0.15. In
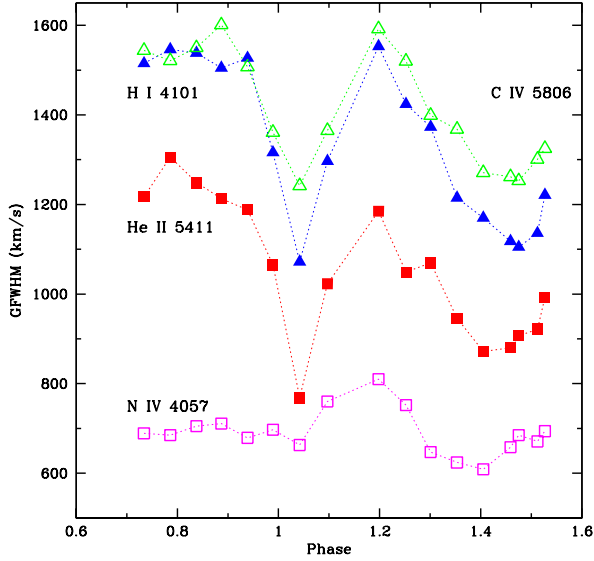
Fig. 3. Full width at half maximum intensity measured with Gaussian fits to the line profiles of NIV 4057 (open squares), He II 5411 (filled-in squares), C IV 5806 (open triangles), H I 4201 (filled-in triangles) in the 1999 spectra. All lines except N IV display the sudden decrease in width when *star A* is "in front" ($\phi \sim 0$). A more gradual decrease is observed at the opposite eclipse ($\phi \sim 0.36$). This is the same behavior seen in the late 1970's. The dotted line connects the data points. Data at eclipse phases correspond to the renormalized spectra.
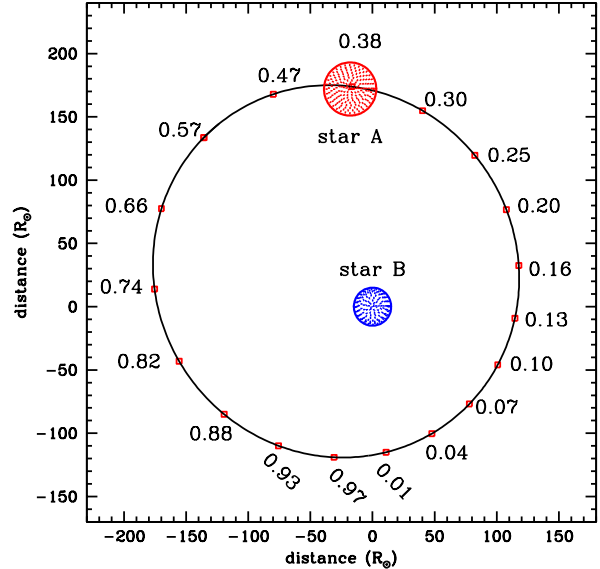

Fig. 4. Schematic representation of the orbit indicating orbital phases in a frame of references in which *star B* is at the origin. For this representation, the masses $M_A=70\ M_\odot$ and $M_B=54\ M_\odot$ (see § 4), and the eccentricity and argument of periastron are, respectively, $e=0.3$ and $\omega=133°$; $R_A=21\ R_\odot$, $R_B=15\ R_\odot$ from BP91. The observer is located off the page at the bottom of the figure.

addition, due to the geometry of the orbit, during the eclipse at $\phi=0.00$ only the wind of *star A* contributes emission or absorption at wavelengths shorter than the rest wavelength.

Figure 4 provides a guide to the location of *star A* with respect to *star B* (located at the center of this coordinate system) as seen by an observer located at the bottom of the page. The squares that are labeled with the orbital phases correspond to the location of *star A* at that given time. Periastron passage occurs near $\phi=0.07$.

3.1. *Emission lines*

With the above ideas in mind, we compared the 2005 FEROS line profiles obtained at orbital phases 0.13, 0.36 and 0.80 with the profiles observed at $\phi=0.00$. The spectrum at $\phi=0.0$ is expected to be dominated by *star A* emission. The individual line profiles are illustrated in Figures 5–10, plotted on a velocity scale corrected for a SMC motion of +150 km s^{-1}. The top left panel contains the $\phi=0$ spectrum. The other three orbital phases are presented in the remaining panels, and compared with the $\phi=0$ profile, which has been shifted in velocity scale to align major features. For example, Figure 5 displays the He II 4542, N V 4603 and N V 4621 Å lines. The velocity shift required to align the maxima of the three emission lines at $\phi=0.13$ is +275 km s^{-1}, while for $\phi=0.8$, the He II 4542 Å emissions are aligned with a shift of -150 km s^{-1}.

We first consider the profiles of N V 4603, 4621 (Figure 5) and the weak He II lines in the $\lambda\lambda6000$–6200 Å region (Figure 6). At $\phi=0.13$ excess emission is apparent in the blue emission line wings, pointed out by arrows. In N V 4603, 4621 Å it can be seen as narrow sub-peaks that "fill in" the P Cygni absorption components. A similar excess emission at this phase appears in N IV 4057, Hδ (Figure 7), Hγ (Figure 8), He II 5411 (Figure 9) and C IV 5806-11 (Figure 10). We interpret this excess blue emission as emission arising in *star B*, which is approaching the observer at $\phi=0.13$.

No relative shift was applied to the spectra at $\phi=0.37$ since the N IV 4057 line coincides almost exactly with the profile of $\phi=0$. In most of the other lines, at least the red wings match very well, but blueward of line center one can easily see that excess emission is present.
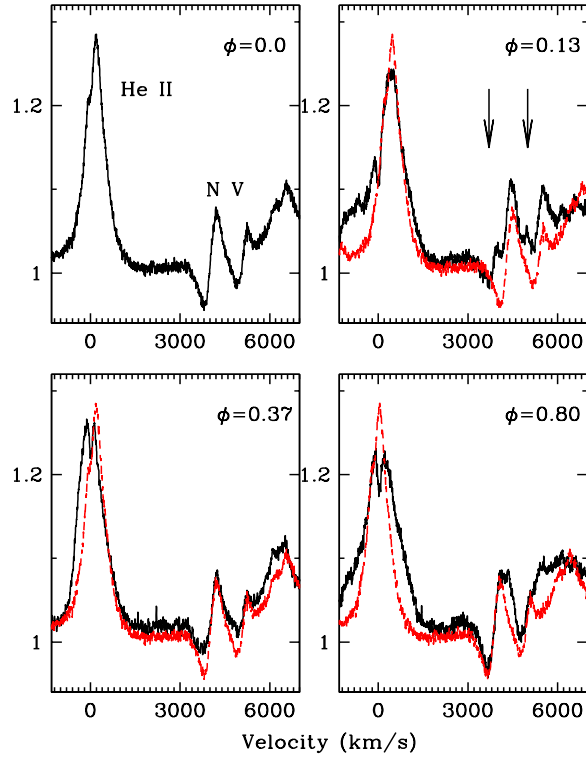
Fig. 5. Line profiles at ϕ=0.0 (top left) used as a template to compare with profiles at ϕ=0.13 (top right), 0.37 (bottom left), and 0.80 (bottom right). The template is shifted by +275 km s^{-1} (top panel, right) and -150 km s^{-1} (bottom panel, right). Spectra at ϕ=0.0 and 0.37 are renormalized to account for the eclipses. The arrows point to excess emission that appears to be associated with *star B*. The velocity scale is centered on the He II λ_0=4541.59 line, corrected for SMC motion (+150 km s^{-1}).

Fig. 6. Same as Figure 5, but for 3 of the He II lines in the 6000-6200 Å region. V=0 km s^{-1} corresponds to λ_0=6100 Å.

At ϕ=0.8 the lines present two different patterns. In the first, N IV 4057, the weak He II 6000-6200 Å emissions and the N V 4603 P Cygni absorptions match the shifted ϕ=0 line profiles. Thus, these features are primarily formed in *star A* and have negative RV's due to its approaching orbital motion. The second pattern, however, is more prevalent and consists of the presence of excess emissions on both wings, although the excess red emission is generally more extended than the blue. Within the context of the interpretation given above, the excess red emission at ϕ=0.8 originates in *star B*, which is receding from the observer at this phase. The excess blue emission, however, appears to arise from an additional source. It is tempting to suggest that it arises from the same source that produces excess emission
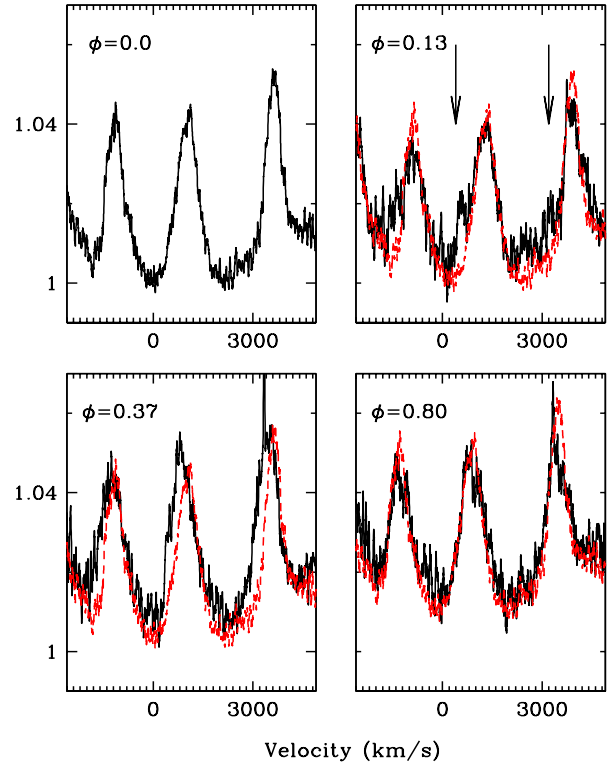
at ϕ=0.36, although its projected velocity towards the observer is greater at ϕ=0.8 than at ϕ=0.36.

Figures 11–14 are grey-scale representation of the 1999 FEROS data and provide a global view of the lpv's in 4 representative lines: N IV 4057, He II 5411, Hβ+He II 4860 and He I 6678 Å. They are constructed with line profile residuals, stacked from bottom to top with increasing orbital phase. The residuals are the differences between each individual spectrum and the average of the 15 spectra obtained over a single orbital cycle and listed in Table 2 (the first two spectra of this table were not included here). The spacing between the spectra is $\Delta\phi \sim 0.05$ in orbital phase, and to consistently retain this spacing in the dynamic plots, the gaps of missing phase coverage are filled-in with grey background color. Plotting the same data twice provides a clearer picture of the orbital-phase dependent trends. The white regions in these images correspond to excess emission; the black to emission deficiency with respect to the mean, or absorption. The maximum dynamic range is typically 10–15% in the residuals with respect to the normalized mean profiles.
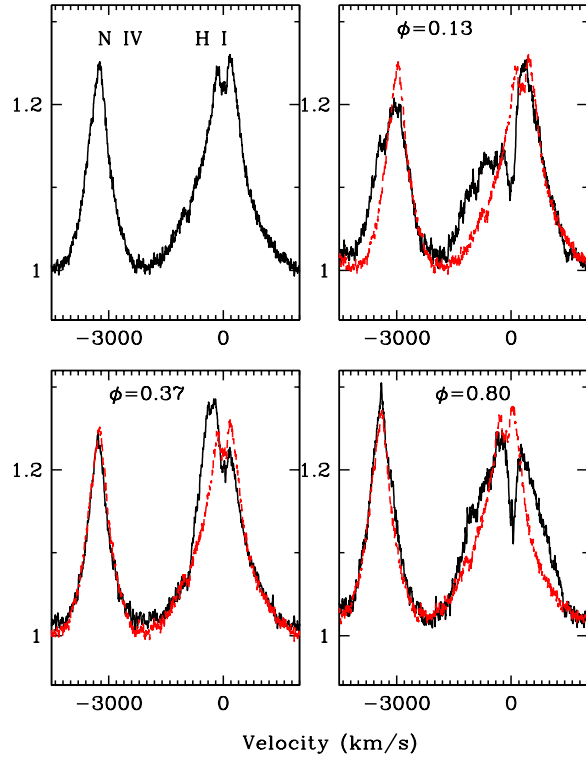
Fig. 7. Same as Figure 5, but for N IV 4057 and H I 4100 Å. Velocity scale is centered on λ 4101.73 Å.

Fig. 8. Same as Figure 5, but for Hγ. Velocity scale is centered on λ 4340.45 Å.

All four dynamic plots display similar large-scale trends; specifically, the excess emission traces out a curve suggestive of orbital motion associated with *star A*. Some of the details of the plots, however, are different. For example, there is a fainter sinusoidal curve that moves in anti-phase with the more dominant bright sinusoid that is clearly seen in He I 6678 and Hβ+He II 4860, is weaker in He II 5411, but not detectable in N IV 4057. In He I 6678, this secondary curve has a "wisp-like" structure around ϕ=0 in the velocity range 0–1000 km s^{-1}. A striking difference between N IV 4057 and H I 6678 is the very extended blue emission in the phase interval $\sim$0.9–1.0 in the latter. While N IV 4057 shows a rapid shift towards the red, as expected from the orbital motion of *star A*, He I 6678 stays very much the same, extending over the velocity range -300 to -1100 km s^{-1}. This implies the presence of emitting gas that is approaching the observer with a speed that is not correlated with the orbital motion within this phase interval.

3.2. *Peculiar behavior of He I P Cygni absorptions*

A clue to the origin of the excess blue emission at ϕ=0.80 may lie in the behavior of the He I lines. As an example, consider the blue wing of He I 5875 Å
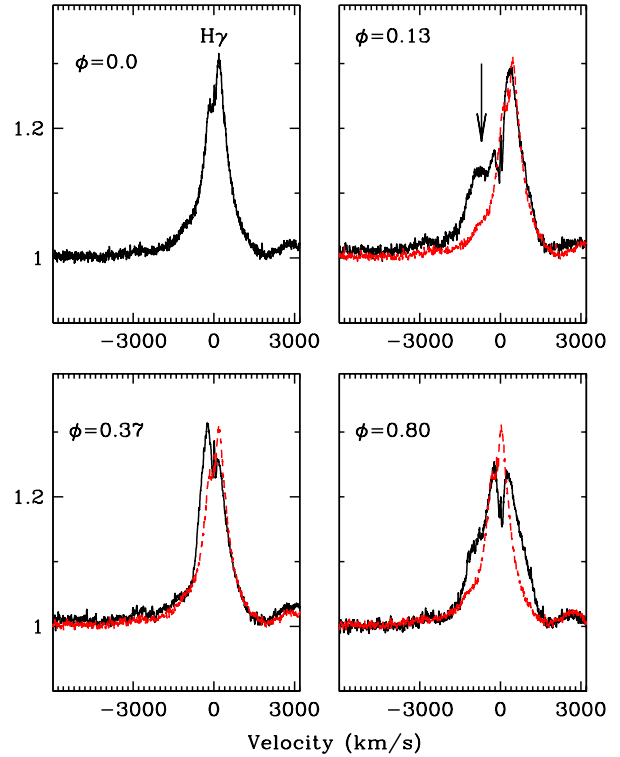
shown in Figure 10. At ϕ=0.80, a sharp P Cygni absorption is present in the same velocity range as the excess blue emission in the H I and He II lines shown in the grey-scale plots discussed above. Such sharp and strong P Cygni absorptions are usually associated with lines formed far from the star, in the low-density regions that are expanding at a constant speed, usually the terminal wind speed, v_{∞}. The presence of the absorption would not be surprising were it not for its *absence* or weakness at other orbital phases. This effect can be more clearly appreciated in Figure 15, which displays montages of He I 4471, 5875, 6678 and 7965 Å at the four orbital phases ϕ=0.0, 0.13, 0.37 and 0.80, and in Figures 16 and 17 where the fuller orbital phase coverage of the 1999 data shows that the absorptions are strongest in the orbital phase interval 0.7–0.9. They nearly vanish at $\phi\sim$0–0.10 (around periastron passage), and re-appear briefly right before the secondary eclipse at ϕ=0.36. They are then very weak or absent (or greatly displaced) between ϕ=0.36 and $\sim$0.7.

There is no immediate explanation for this behavior, although similar features have been linked to the WWI interface in the well-documented case of V444 Cygni (Marchenko, Moffat, & Koenigsberger
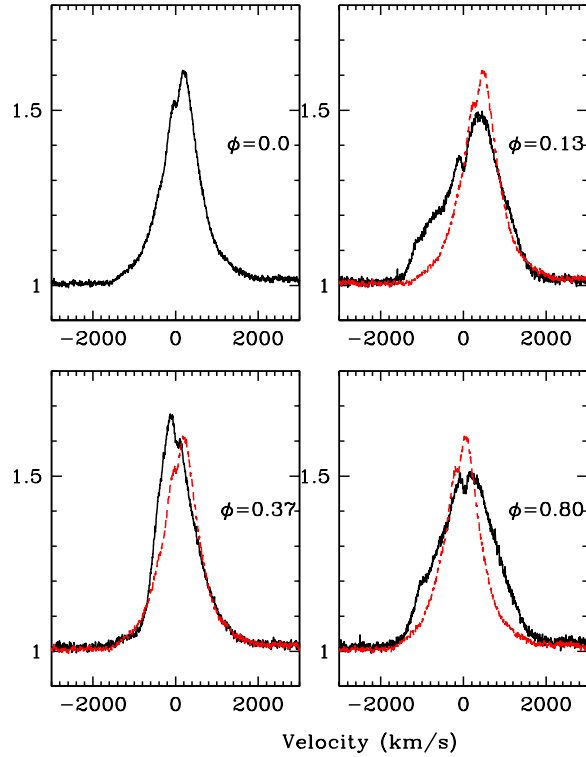
Fig. 9. Same as Figure 5, but for He II 5411 Å. Velocity scale is centered on λ 5411.52 Å.

Fig. 10. Same as Figure 5, but for He I 5875.80 Å.

1994; Marchenko et al. 1997), in GP Cep (Demers, Moffat, & Marchenko 2002), in γ^2 Vel (De Marco 2002), and in η Carinae (Nielsen et al. 2007). It is also interesting to note that in these four systems the observations lead to the conclusion that there are substantial differences in strengths and velocities of the leading/trailing WWC arms. A similar scenario for HD 5980 will be discussed in § 8.

In summary, we find that the only lines in the optical spectrum of HD 5980 that are likely to truly describe the orbital motion of *star A* are N IV 4057, N V 4603 and some of the weak He II lines in the $\lambda\lambda$6000–6200 Å range.

4. NEW CONSTRAINTS ON THE MASSES OF THE SYSTEM

The top panel of Figure 18 illustrates the RV curves that result when the centroid of the emission lines is measured using a single Gaussian fit. The corresponding data are listed in Columns 4, 7 and 10 of Tables 2 and 3. The RV curve for N IV 4057 Å line is very similar to that derived by Barbá et al. (1997), indicating that *star A* is still the major contributor to this line. The H I + He II 4101 and He
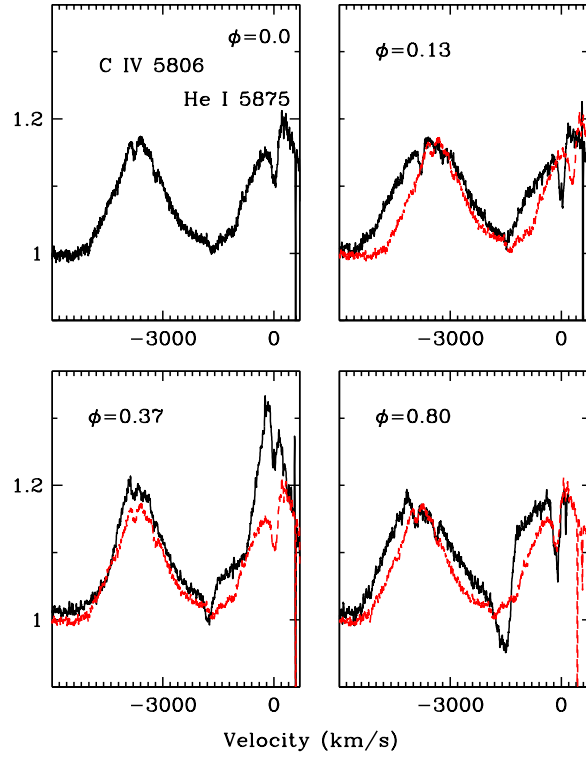
II 5411 Å display a similar trend, but with different amplitudes and shapes, implying that they contain a more significant contribution from *star B* and from the WWI region.

Assuming that the line profile variability is in part due to the superposition of emission arising in two distinct sources, we deblended the lines using a two-function fit to the profiles. The results of these measurements are plotted in the middle and bottom panels of Figure 18 (filled-in pentagons), showing two RV curves in anti-phase. Using a similar procedure, we deblended the N V 4603 emission (open stars) using two Gaussians. The results for N V are more uncertain for two reasons: (1) the P Cygni absorption component of the neighboring N V 4621 Å line limits the extent of the N V 4603 Å red wing; (2) at ϕ=0.13, *star B*'s component is shifted into *star A*'s P Cygni absorption component. On some spectra, this superposition makes it very difficult to measure the secondary component, since it simply fills in the P Cyg absorption but is not prominent enough to enter the two-function fit. Because *star A*'s contribution is dominant, its RV curve is not severely affected by these two effects. However, that of *star B* not only displays much larger scatter, but also a systematic deviation from the RV curve derived from
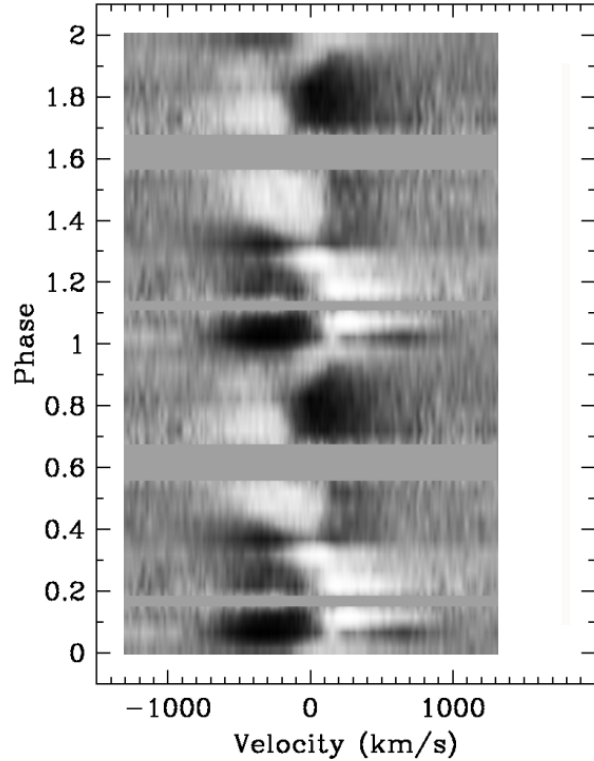
Fig. 11. Grey scale representation of residuals for N IV 4057. Phase increases from the bottom to the top, the same data being plotted twice. White corresponds to positive residuals, black to negative. Residuals are the difference between the nearly equally-spaced (in phase) 1999 FEROS spectra and the average of these same spectra. Gaps in phase coverage are filled in with grey background color.

Fig. 12. Grey scale representation of 1999 FEROS data for He II 5411 as in previous figure.

N IV 4057. Part of this deviation may also be due to NV emission arising in the WWI region.

The middle panel of Figure 18 also contains the RV variations of the weak He II 6074.1 and He II 6118.2 Å lines (small open squares), obtained by fitting a single Gaussian function. These lines show a slightly smaller RV amplitude than that of N IV 4057 Å, consistent with the notion that they arise primarily in the wind of *star A* but also contain a contribution from *star B*.

The shape of the RV curve of *star B* shown in the bottom panel of Figure 18 matches quite well the mirror of the RV curve for *star A*, within a constant factor (related to the relative masses of the two stars), thus supporting the hypothesis that the excess emission (with respect to the $\phi=0$ spectrum) is in fact primarily coming from these stars. The WWI excess should be out of phase with the orbital motion.
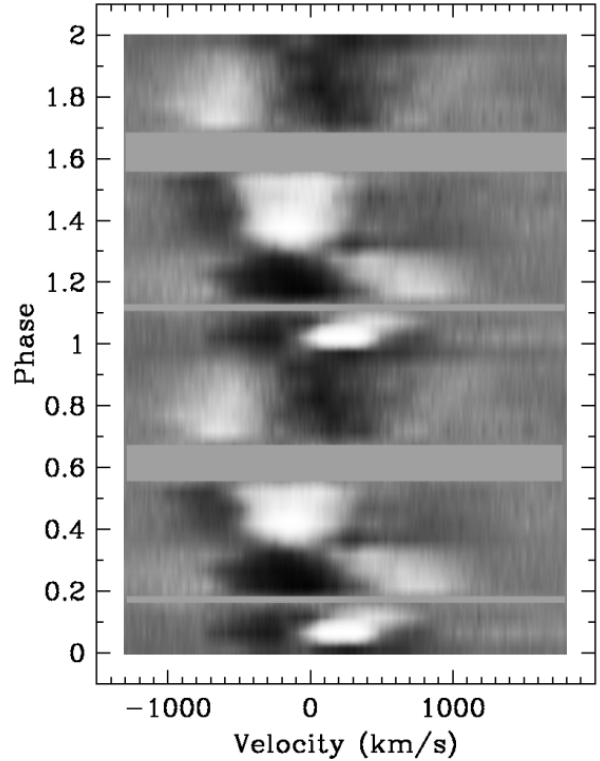
We performed a fit to the RV amplitude of NIV and NV using the genetic algorithm PIKAIA (Charbonneau 1995). The radial velocity curves of the two stars were fitted simultaneously, giving the two RV semi-amplitudes (K1 and K2), the eccentricity e, and the longitude of the periastron ω_{per}. The semi-amplitudes are K_{A}=198 km s^{-1} (NIV) and 180 km s^{-1} (NV), and K_{B}=222 km s^{-1} from both lines. These results lead to M_{A}=58–79 $M_{\odot}$ and M_{B}=51–67 $M_{\odot}$, adopting an orbital inclination angle i=88° (Moffat et al. 1998) and given the uncertainties in the fit to the RV curves (±4 km s^{-1} and ±16 km s^{-1} for *star A* and *star B*, respectively). The corresponding range in semimajor axis is a=143–157 $R_{\odot}$. The orbital eccentricity derived from both N IV and NV solutions is e=0.30$\pm$0.16. This value is compatible with e=0.27 (Moffat et al. 1998) and e=0.32 (BP91). The longitude of periastron that we derive lies in the range ω_{per}=283°–294°. This is smaller than the corresponding values of ω_{per}=319°$\pm$6 (Moffat et al. 1998) and ω_{per}=313° (BP91). Given that the RV curve has a limited orbital phase coverage and that various interaction effects are present in the emission-line spectrum, we favor the values of
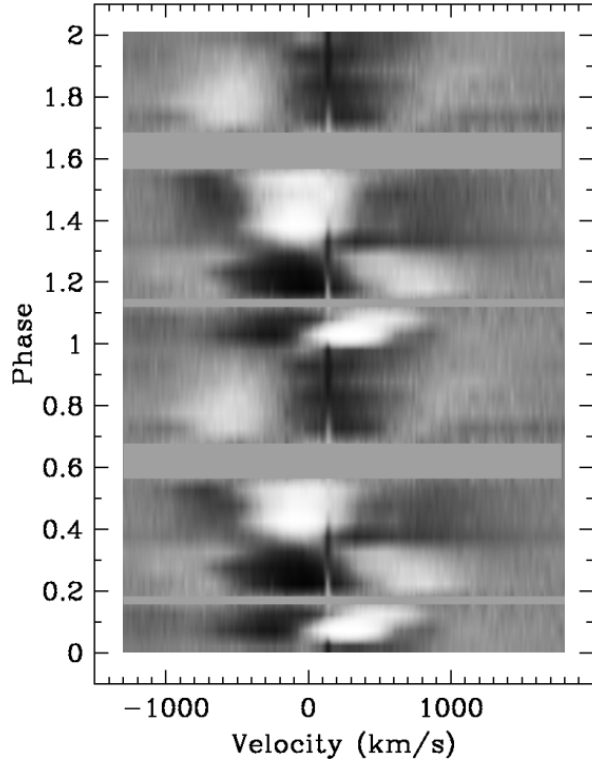
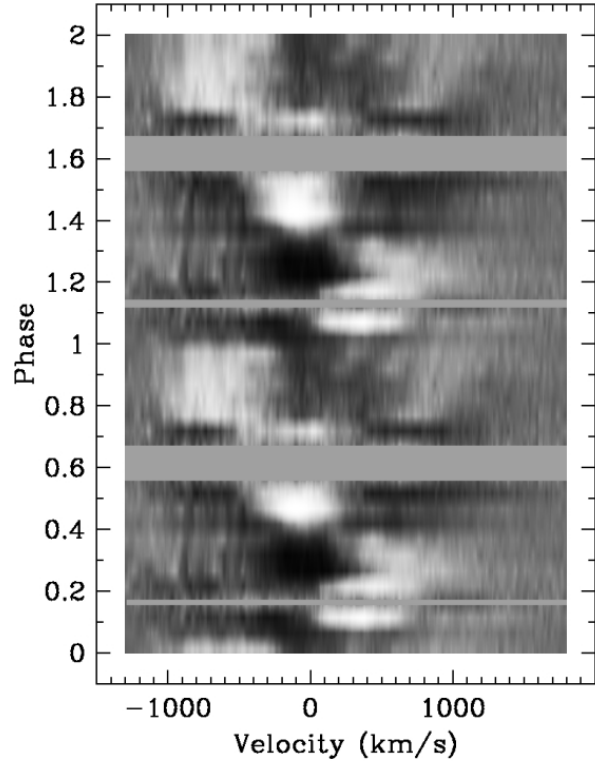Fig. 13. Grey scale representation of 1999 FEROS data for Hβ+He II as in previous figure.

Fig. 14. Grey scale representation of 1999 FEROS data for HeI 6678 as in previous figure.

ω_{per} derived from the photometric light curve and polarimetry (BP91; Moffat et al. 1998).

The above masses are significantly larger than those based on single function fits to the emission lines and they are more consistent with the stars' position on the H-R Diagram near the 120 $M_\odot$ evolutionary track (Koenigsberger 2004).

5. DECLINING WIND DENSITIES?

The emission lines in 2005 are substantially weaker than observed in 1999, indicating that the trend for decreasing wind densities that was observed in UV spectra (Koenigsberger 2004) is continuing. In order to quantify the effect, we measured the equivalent width (EW) of H δ+HeII 4101 Å, NIV 4057 Å, and He II 5411 Å as listed in Tables 2 and 3. The orbital phase-dependent variability in 1999 is plotted in Figure 19, showing that He II 5411 Å displays a large modulation with a broad minimum centered around $\phi{\sim}0.15$, while N IV 4057 Å gives only a hint of an eclipse at ϕ=0.36. No clear phase-dependent changes are evident in Hδ+He II 4101 Å. Figure 20 illustrates the ratio EW(He II 5411)/EW(Hδ+He II 4101) as a function of orbital phase for the two different epochs, 1999 and 2005, leading to the conclusion

that the degree of ionization in HD 5980 was greater in 2005 than in 1999. Consistent with this conclusion is the significanly weaker N III 4640 Å blend in 2005 compared to that of 1999.

Hence, these are indications that HD 5980's wind is reverting to its state prior to the 1993/1994 eruptions, when the emission lines were much broader and significantly weaker (Koenigsberger et al. 1998a; Moffat et al. 1998).

6. STATIONARY PHOTOSPHERIC ABSORPTIONS

A striking feature in the 2005 FEROS data is the strength of photospheric absorptions clearly seen superposed on the emission lines (see, for example, Figures 2, 7, 8, 10, and 15). Similar absorptions have been observed in 1999 HST/STIS spectra (Koenigsberger, Kurucz, & Georgiev 2002), and found to be relatively stable in wavelength; that is, the amplitude of the RV variations was $\leq$40 km s^{-1}, which was within the uncertainties of the RV measurements. Table 6 lists the dominant absorption lines that we identified in the 2005 FEROS data, with measurements of their RV (Columns 2, 4, 6, and 8) and

TABLE 6

PHOTOSPHERIC ABSORPTIONS 2005

Atomic ID	$\phi=$ 0.8 RV	0.8 FW	$\phi=$ 0.0 RV	0.0 FW	$\phi=$ 0.13 RV	0.13 FW	$\phi=$ 0.37 RV	0.37 FW
He I 3819.60	142	175	190	286	–	–	?	?
H 9 3835.38	167	260	170	214	186	224	140	267
	–	–	–	–	−120	468	–	–
He I 3888.64[c]	208	282	198	207[a]	163	264	195	201
He I 4026.18	182	178	153	119	154	171	144	127
	–	–	–	–	−324	554	–	–
H I 4101.76:	194	265	176	213	157	239	156	221
	–	–	–	–	−314[b]	579	–	–
He II 4199.84[d]	174	278	176	164	171	176	166	186
	–	–	–	–	−249	547	–	–
H I 4340.49	163	220	135	232	141	247	141	185
	–	–	–	–	−351	406	–	–
He I 4387.93	149	276	175	137	188	326	170	189
He I 4471.50:	168	185	167	152	161	158	155	132
He II 4541.59	190	181	192	126	165	137	168	183
–	–	–	–	–	−249	545	–	–
H I 4861.30	176	287	113:	311	141	257	188	326
He I 4921.93	165	207	173	163	156	166	155	178
He I 5015.68	181	144	179	148	173	160	167	123[b]
He II 5411.52	181	178	197	128	177	141	189	125
	–	–	−142	145	−323	400	–	–
O III 5592.4	166	150	156	149	168	134	148	117
C IV 5801.3	178	177	203	180	165	141	182	170
C IV 5812.0	177	132	200	117	199	136	–	–
He I 5875.8	173	220	164	190	162	180	162	160
He I 6678.15	436	181	187	113	122	250	–	–
	–	–	−145	324	419	151	–	–
He I 7065.71	150	250	154	199	147	234	141	129
	–	–	–	–	−549	569	–	–
N IV 7111.28	152	93	170	105	129	73	136	74
	8	156	–	–	–	–	–	–
N IV 7122.98	277	110	–	–	–	–	–	–
	16	81		–	–	–	–	–
<>	172	–	173	–	161	–	161	–
s.d.	±16	–	±22	–	±19	–	±18	–

[a]Filled-in by emission.

[b]Very clear.

[c]Blended with H I 3889.05.

[d]Blended with N III 4200.

their corresponding FWHM (Columns 3, 5, 7, and 9), measured with Gaussian fits to the profiles. It is important to note that since these features are superposed on strongly variable emission lines, the extent of the absorption line wings is nearly impossible to establish. Hence, the RV measurements refer to the line cores and these do not display any significant RV variations. In fact, if we average the RV values for each orbital phase listed in Table 6, we find that the average RV values are virtually constant, within the standard deviation of the measurements at each orbital phase. The averages and standard deviations are listed in the bottom rows of Table 6. The average velocity at each of the four orbital phases listed in this table are within the range 161–172 km s^{-1}, with a corresponding range in standard deviations of ±16 to ±22 km s^{-1}. Hence, they are indeed stationary within the timescale of the 2005 observations.
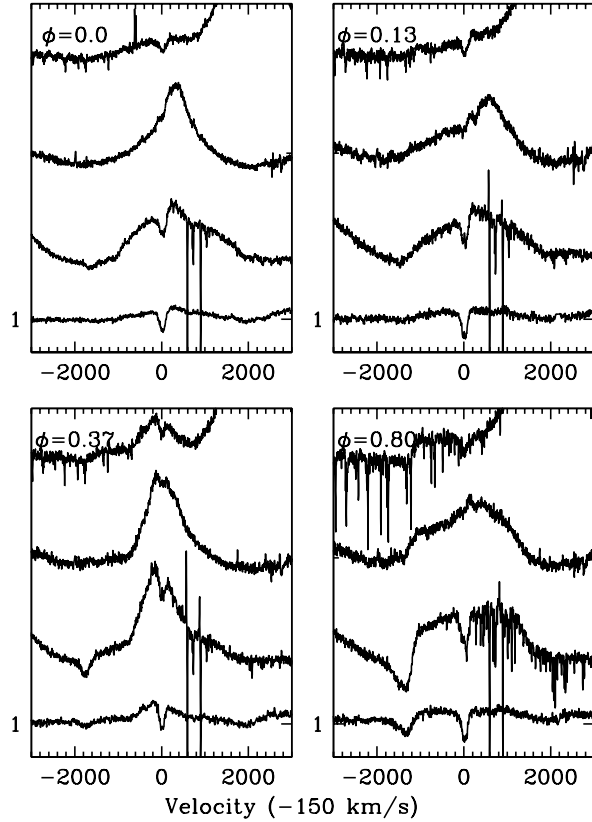
Fig. 15. FEROS 2005 line profiles of He I 7065, 6678, 5875 and 4471 Å (from top down). The spectra are averages for each of the orbital phases ϕ=0.0 (top left), 0.13 (top right), 0.37 (bottom left) and 0.80 (bottom right). At ϕ=0.0 and 0.37 they are renormalized to account for the eclipses. The velocity scale is corrected for the +150 km s^{-1} systemic velocity of the SMC. Note that the photospheric absorption lines are stationary. The P Cygni absorptions are particularly prominent at ϕ=0.80.
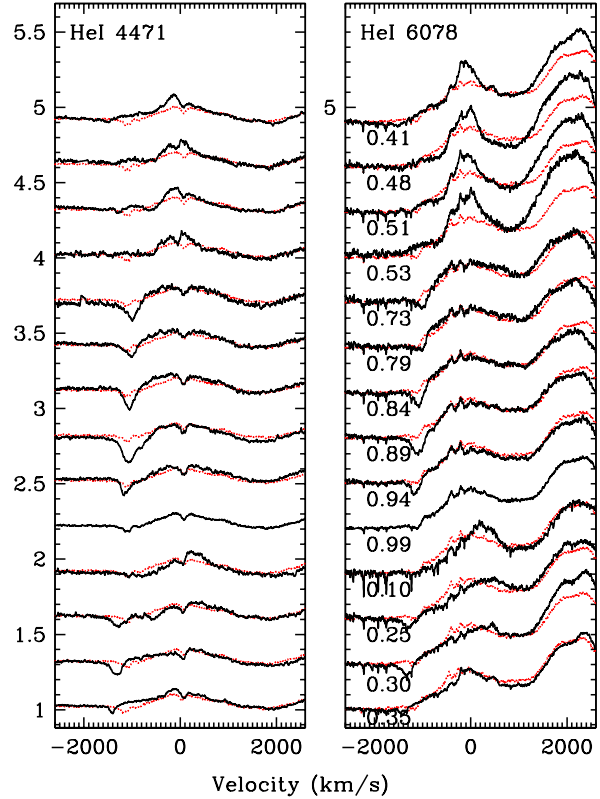
Fig. 16. Montage of the 1999 individual FEROS spectra obtained over a single orbital cycle illustrating the behavior of the He I P Cygni absorption components. The template (dotted spectrum) is the profile at ϕ=0.99, renormalized to account for the eclipse. The spectrum at ϕ=0.35 is also renormalized. The absorption is strong during the phase interval ϕ=0.73–0.30, but nearly vanishes at ϕ=0.99 (eclipse of star B). The y-axis is relative intensity, each spectrum having been shifted along this axis by 0.3 units. The x-axis is velocity with respect to the laboratory wavelength, corrected for SMC systemic motion (+150 km s^{-1}).

The photospheric absorptions are believed to arise in *star C* (Niemela 1988; Koenigsberger et al. 2001) which is a reasonable conclusion, given their apparently stationary nature over the P=19.2654 day orbital timescales. Over longer timescales, however, the RV and strength of the lines undergo changes, as illustrated in Figure 21, where the He I 4471 Å lines observed in 1999 and 2005 are compared. At each of the four orbital phases plotted in the figure, the 1999 profiles are significantly redshifted with respect to those of 2005. Schweickhardt (2000) measured the RVs of the O III 5592.4 photospheric absorption line in 1999 FEROS data, finding them to be periodic with $P_{\rm starC}$ ∼96.5 days, and suggested that *star C* is itself a binary system. His analysis of the RV curve implies that the *star C* system is

very eccentric (e=0.83; ω=255°; T_0=2451183.6) and that the amplitude of the star responsible for the O III photospheric absorption is K=71 km s^{-1}. Similar results were derived from the analysis of the He I 4471 Å photospheric absorption. Our 2005 data only cover a fraction of the phase for such a period, $\phi_{\rm starC}$∼0.4–0.8, which lies in a relatively constant portion of the *star C* RV curve. However, OIII 5592.4 RV variations do show a declining trend with total amplitude of ∼20 km s^{-1} which is consistent with Schweickhardt's (2000) conclusion. If this binary is gravitationally bound to the A+B pair or whether it is merely a line-of-sight projection remains to be resolved. In any case, however, Schweickhardt's (2000)
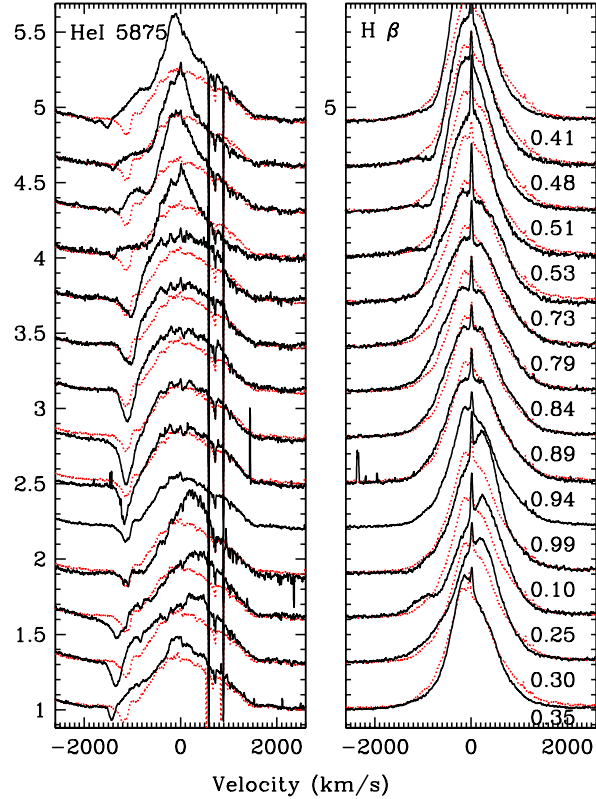
Fig. 17. Same as previous figure, but for He I 5875 Å (left). The same behavior is observed for the P Cygni absorptions. Note that when they are sharpest and strongest, the emission component has a very rounded shape. When the P Cygni absorption is not as prominent, the emission appears to have a sharper (possibly superposed) additional emission component. The right panel illustrates the same montage of spectra at Hβ. The y-axis is relative intensity, each spectrum having been shifted along this axis by 0.3 units. The x-axis is velocity with respect to the laboratory wavelength, corrected for SMC systemic motion (+150 km s^{-1}).
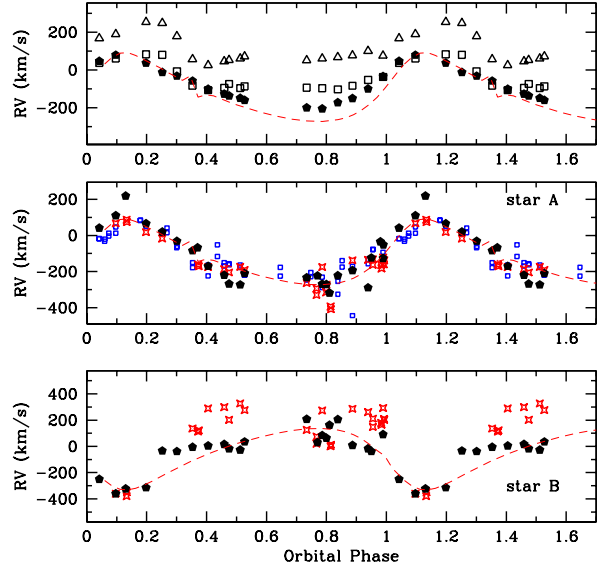

Fig. 18. Radial velocity measurements. Top: A single Gaussian was fit to lines of N IV 4057 Å (filled pentagons), H I 4101 Å (squares) and He II 5411 Å (triangles). Each RV curve has a different shape due to contributions from different sources. Middle: *Star A*'s contribution isolated using a 2-function fit to N IV 4057 Å (filled pentagons) and N V 4603 Å (stars), and a single Gaussian to He II 6074 and 6118 Å (small squares). Arbitrary vertical shifts were applied to correct for different zero-point locations and align the 4 RV curves. Bottom: *Star B*'s deduced contribution derived from the 2-function fit to N IV 4057 Å (filled pentagons) and N IV 4603 Å (stars). The dashed curves are theoretical computations for a 70+54 $M_\odot$ binary system in an e=0.3, ω=133° orbit. All RVs are corrected for the SMC systemic velocity (+150 km s^{-1}).

results suggest that *star C* is also an intriguing object that requires further analysis.

An explanation of why the photospheric absorption lines appear to be more prominent in 2005 compared with 1999 may lie in the decreasing visual brightness of *star A* which thereby makes *star C*'s photospheric absorptions appear more prominent. Another possibility is that since the emission lines became weaker in 2005 compared with 1999, photospheric absorptions from *star A* could enhance the strength of absorptions in the combined spectrum.

In Table 6 we have also listed the measurements of a photospheric-like dip observed at orbital phase ϕ=0.13 "blue-ward" of the stationary absorptions.

It is typically located at −500 km s^{-1} from the stationary absorptions, with a FWHM∼500 km s^{-1}. At this phase, *star B* is approaching the observer and it is conceivable that these broad features could be associated with its photospheric absorptions. The large width and the excess blue-shift (with respect to the orbital motion) could be produced by the velocity gradient in its photosphere. An alternative explanation may reside in the presence of a slower-moving wind region (or WWI region?) projected upon the stars at this phase. However, this issue must await further observations since, as the intensity of the emission lines from *star A* diminishes, the characteristics of photospheric absorptions will become easier to establish.
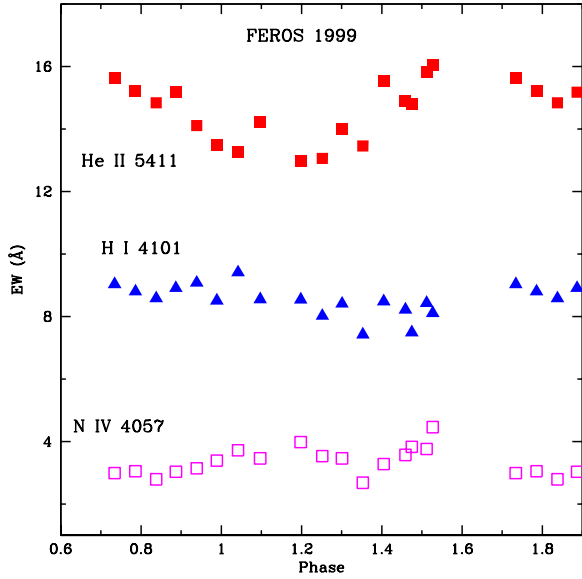
Fig. 19. The equivalent width of 1999 FEROS data as a function of orbital phase for N IV 4057 Å Hδ+ He II 4101 Å and He II 5411 Å.
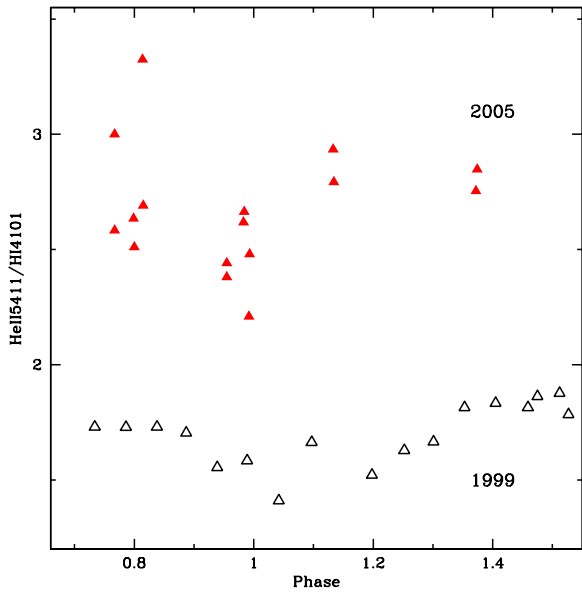

Fig. 20. The ratio of equivalent widths of He II 5411 Å and H I (+He II) 4101 Å as a function of orbital phase for the 1999 and 2005 FEROS observations. There is only a hint of an orbital-phase dependence in 1999. Much clearer is the overall change in the ratio from 1999 to 2005, indicating that the degree of ionization increased in 2005.

7. LIGHT CURVE

Figure 22 illustrates four sets of HD 5980 photometry. The best full orbital phase coverage (open
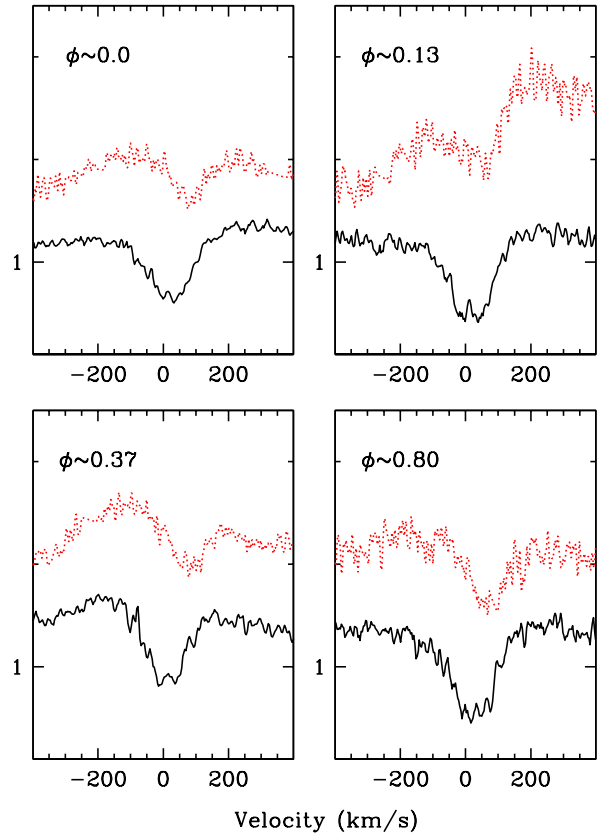

Fig. 21. Comparison of the He I 4471 Å photospheric absorption line in the 1999 (dotted) and in 2005 at four orbital phases. The velocity scale is corrected for an assumed SMC systemic velocity of $+150$ km s^{-1}, and the 1999 data were shifted upward for clarity in the figure. Note that the 2005 profiles are blue-shifted and stronger than the 1999 profiles. The 1999 spectra were obtained over the timescale MJD 51381.4-51391.4.

squares) consists of visual magnitude observations obtained using the CTIO/SMARTS telescope during 2005. The second set having full phase coverage consists of the original BP80 differential magnitudes (crosses), with a constant value of 10.415 mag added in to make the average levels coincide with those of the SMARTS and the Swope data at orbital phase 0.60. The Swope data (small plus signs) have a poorer overall phase coverage, but cover portions of the ascending branch of the $\phi=0.36$ eclipse more densely. Finally, the Danish telescope differential magnitudes to which the constant value of 12.57 mag has been added (triangles) are primarily concentrated around $\phi=0.99$ and around the $\phi=0.36$ eclipse phase. The top panel of Figure 22 illustrates the complete light curve, while the middle and lower panels focus on the two eclipses.
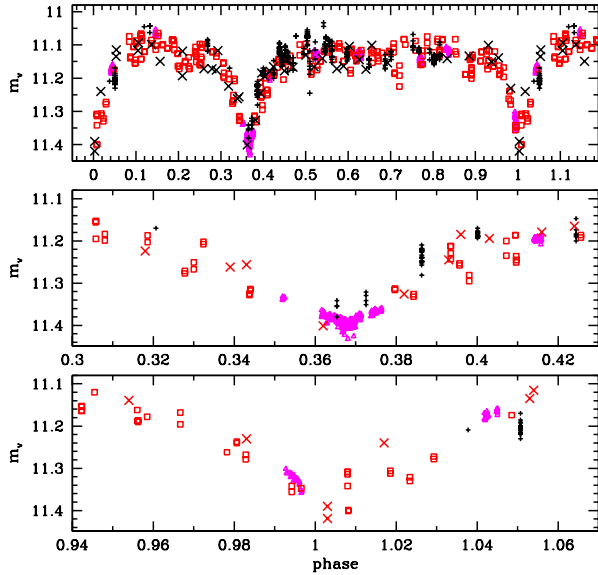
Fig. 22. Visual magnitudes from SMARTS (open squares) and Swope (plus signs) compared with differential photometric observations of Breysacher & Perrier (1980; data of July-October 1979) +10.415 mag (crosses); and Danish data +12.57 mag (filled-in triangles). Orbital phases for the Danish2005, SMARTS and Swope data sets were computed using T_0=JD2443158.705 and P=19.2654 days from Sterken & Breysacher (1997). The orbital phases of BP80 data are as listed in their Table 1, which BP80 computed with T_{BP80}=JD2443158.771 and P_{BP80}=19.266 days. The difference in phase computed with P and P_{BP80} is <0.002 for the BP80 data.

Fig. 23. Differential photometric observations from the Danish telescope at ϕ=0.36–0.37, after adding +12.57 mag to convert to visual magnitudes consistent with the SMARTS values. Top: plotted as a function of time (in hours). Bottom: plotted as a function of orbital phase, using P=19.2654 d and $T_{modified}$=JD2443158.865. With this $T_{modified}$, the secondary minimum is centered on ϕ=0.36. The error bars correspond to the uncertainty per individual data point, σ_{instr}.

The difference between the 2003 (SWOPE) and 2005 SMARTS data sets during the ascending branches of both eclipses (there are practically no 2003 data during the descending branches) is noteworthy. It shows the large degree of epoch-to-epoch variability in the system. Also, we should note that in order to shift the photometric minimum to the anticipated ϕ=0.36, a slightly corrected $T_{modified}$=2443158.865 is suggested, which also better accommodates the photometry obtained in 1994–1995 (Moffat et al. 1998). This implies a significantly larger difference with respect to the Sterken & Breysacher (1997) T_0=2443158.707±0.07 than their quoted uncertainty. The possibility that this shift is related to apsidal motion and a full analysis of the eclipse light curve will be explored in a forthcoming investigation. It is important to note that the analysis requires the methodology used by BP91 in which the extended nature of the continuum eclipsing sources is contemplated.
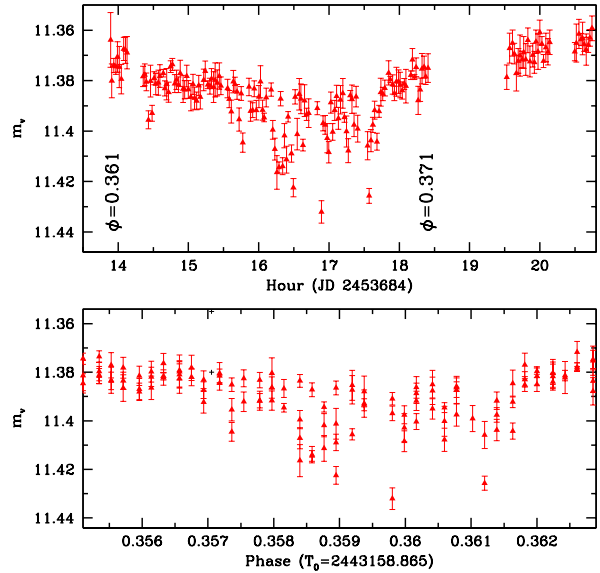
The longest train of Danish data was obtained around eclipse at ϕ=0.36–0.37, and the individual data points are plotted in Figure 23, disclosing $\sim$0.^{mag}035 amplitude variations within a timespan of half an hour. This is considerably shorter than the $\sim$6-hour periodic variations (0.02 mag) reported by Sterken & Breysacher (1997) and attributed to oscillations of $star\ A$. Curiously, if we assume T_0=$T_{modified}$=JD 2443158.865, then the two prominent minima appear symmetrically located around $\phi_{modified}$=0.36 (where $\phi_{modified}$ is the phase computed using the modified value of T_0). This would seem to indicate the presence of a bright emitting source that is eclipsed just prior to and just after mid-eclipse, but not during mid-eclipse. Or, alternatively, the presence of dense, eclipsing gas located at a distance from $star\ B$ slightly larger than the radius of $star\ A$. One geometry for such a gas that comes to mind is that of a WWI interacting region whose apex is transparent to optical radiation.

Strong variability near ϕ=0.36 on similar timescales has previously been reported in polarimetric observations (Villar-Sbaffi, Moffat, & St.-Louis 2003), and two HST/STIS UV observations

obtained one day apart at these same phases suggest that the wind speeds are very variable.

8. THE WIND-WIND INTERACTION REGION

The current view of the HD 5980 system, consisting of two stars with powerful winds, implies the presence of an interaction zone. Thus, at least part of the variability reported in this paper may result from phase-locked wind-wind interaction effects. In its simplest representation, the WWI region can be modeled in terms of a discontinuity between the two winds that consists of the two thin shocks formed when the supersonic winds collide and whose shape depends on the momentum ratio of the stellar winds. Figure 24 is a cartoon illustrating the WWI region shape for HD 5980, assuming that the wind of *star A* dominates. This assumption is based on the fact that all emission lines in the combined spectrum increased significantly in strength after the 1994 eruption and that the phase of their Doppler motions corresponds to that of *star A* (Koenigsberger 2004). The significantly larger emission measure from *star A* compared to *star B* is expected to correlate with a larger density. Preliminary stellar wind models for the HD 5980 system that have been fitted to FUSE 2002 data imply that *star A*'s mass-loss rate was still large, $\dot{M}_A \sim 10^{-4}$ $M_\odot$ yr^{-1} (Georgiev et al., in preparation). In addition, for *star B*, Moffat et al. (1998) found $\dot{M}_B = 2 \times 10^{-5}$ $M_\odot$ yr^{-1} from polarimetric data obtained prior to the eruption. These mass-loss rates, combined with wind terminal speeds derived from UV and FUV observations lead to the WWI shock cone configuration shown in Figure 24, with a shock cone opening angle $\sim 50°$.

Four orbital phases are shown. *Star A* is represented with three concentric circles depicting, respectively, its photosphere (R_A), the extent of its accelerating wind region in the case of a "fast" velocity law (~ 1.5 R_A), and the extent of the dominant emitting wind region for a moderately strong, but arbitrary, emission line (~ 4 R_A). Note that because the orbit is eccentric, the WWI discontinuity intersects the line emitting region around periastron passage, but not around apastron. When the WWI region intersects the line-emitting region, the intensity of the observed line-profile is truncated at the corresponding velocity range. The sets of dashed lines drawn parallel to the line-of-sight in Figure 24 enclose columns of wind material that are projected against the luminous stellar continua and that are expanding towards the observer (located at the bottom of the figure). All P Cygni absorption components observed in the spectrum arise in these columns.
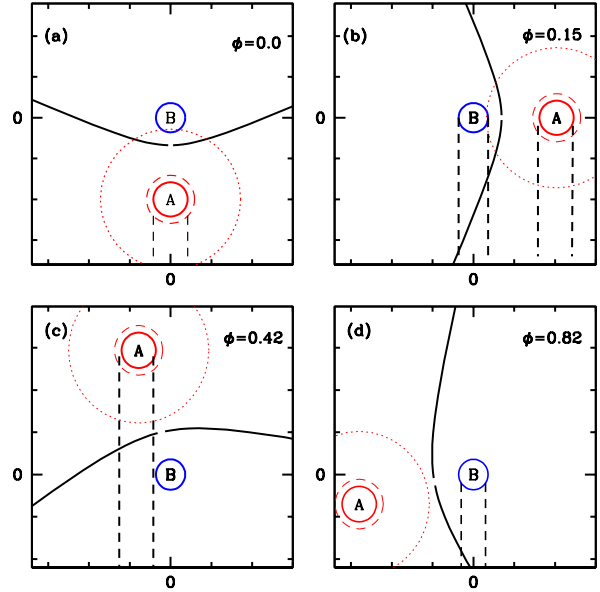

Fig. 24. Cartoon of the system geometry for different orbital phases, illustrating how the lines-of-sight to the two stars cross different portions of the WWI region and the stellar winds. Dashed lines contain the columns of gas projected onto the continuum-emitting regions, as seen by an observer situated at the bottom of the page. Discontinuous circles around *star A* indicate the accelerating portion of the wind ($1.5R_A$) and the assumed extent of a line-emitting region ($\sim 4R_A$).

The behavior of the blue-shifted, sharp absorption components of the He I emission lines suggests that they arise in the WWI region. They are strongest during the orbital phase interval 0.7–0.9 (when both stars are in view and one of the WWI arms lies in the foreground of *star B*) and they are weak at $\phi \sim 0$–0.10 (when mostly *star A* is in view) and $\phi = 0.36$–0.7 (when mostly *star B* is in view). It is important to note that the sharp and deepest portion of the P Cygni absorption components generally arise in the wind regions that have attained terminal speeds. In the 1999 data, at orbital phase ~ 0.8, the He I 4471 Å sharp feature extends between -900 to -1340 km s^{-1}, and maximum absorption at ~ -1130 km s^{-1} (assuming a correction for SMC motion of -150 km s^{-1}). This is significantly slower than terminal wind speed of -1750 km s^{-1} inferred for *star A* during the same epoch from HST/STIS observations of UV lines (Koenigsberger et al. 2000). This slower speed is qualitatively consistent with absorption of *star B* radiation traversing the foreground WWI region arm. Also noteworthy is the fact that excess blue-shifted emission appears in many lines around orbital phase $\phi = 0.36$, which is tempting to
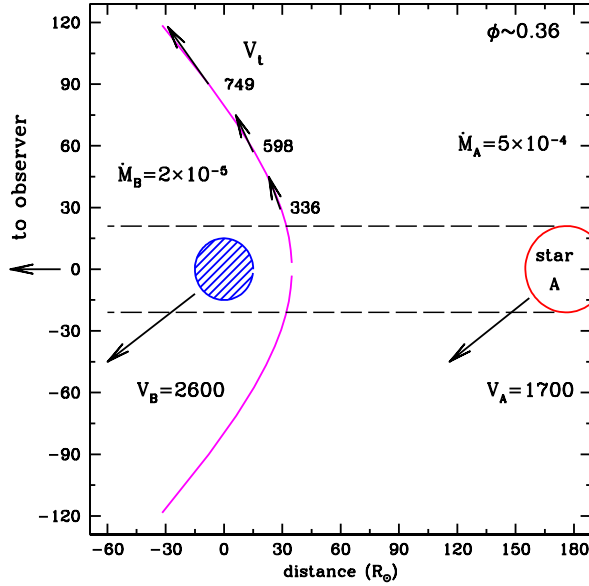
Fig. 25. Schematic representation of the WWC shock cone at orbital phase 0.36 listing tangential flow velocities (v_t) computed using the relations given by Cantó et al. (1996). The assumed mass-loss rates are given in $M_\odot$/year and the velocities in km s^{-1}. The observer is off the page to the left at ϕ=0.36. The dashed lines contain the column of material traversed by the line-of-sight from the observer to *star A*. With the assumed radii (R$_A$=15 $R_\odot$ and R$_B$=21 $R_\odot$), the light from *star A*'s disk must pass through the WWI region *and star B*'s inner wind before reaching the observer. Time-dependent mass ejections from *star B* or instabilities along the WWI region could be responsible for the rapid variability observed at this orbital phase.

attribute to emission arising in the WWI zone that is not projected against either continuum source.

Figure 25 provides estimates of the flow velocities, V_t, along the shock cone walls derived from the expressions given by Cantó, Wilkin, & Raga (1996), using the roughly estimated values for mass-loss rates of the two stars. At orbital phases around 0.8, the line-of-sight from the observer to *star B* crosses regions of the WWI having $V_t \sim$600–800 km s^{-1}. Considering that the shock cone has an opening angle $\sim$50°, the maximum projected speed of V_t along the line-of-sight in the stationary frame of reference is $\sim$−600 km s^{-1}. This is significantly smaller than the speeds at which the He I P Cygni absorption components are being observed. Correcting for the orbital motion of *star B* of $\sim$220 km s^{-1} brings the predicted value closer to the observations at $\phi\sim$0.15, when *star B* is approaching the observer, but increases the discrepancy round $\phi\sim$0.8. However, the
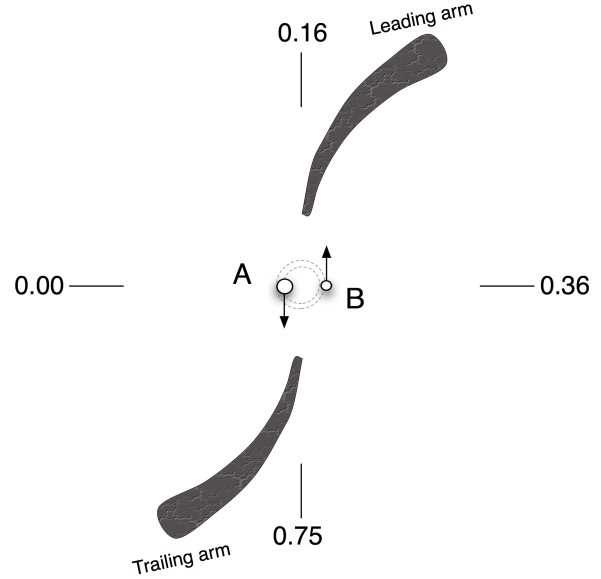

Fig. 26. Cartoon illustrating an alternative geometry for the WWI region that would be consistent with the orbital phase-dependent behavior of the He I P Cygni absorption components.

idealized WWI model presented in Figures 24 and 25 is a greatly simplified model. For example, if we take into account that the axis of symmetry for the WWI shock cone is in reality tilted with respect to the line connecting the two stars, the angle between the leading WWI arm and the line-of-sight decreases, allowing for faster projected speeds. In addition, numerical simulations that include orbital motion show that the shock cone arms are curved. Hence, the leading and the trailing arms could cross the line-of-sight to the stars at different orbital phases and with larger projected speeds than depicted in Figure 25. Figure 26 is a cartoon that illustrates an alternative geometry for the WWI region, based on an interpretation of the variable He I P Cygni absorption lines. It would be interesting to analyze whether the physical mechanisms involved in the WWI can give rise to such a different geometry, compared to the typical conical surfaces that are predicted by the traditional calculations.

It is important to keep in mind that the geometry and characteristics of the interaction region depend on whether the shocked gas is radiative or not, and this, in turn, determines the intensity and shape of line emission/absorption that the WWI region can produce. One can estimate whether the gas is radiative or not using the parameter χ from Stevens, Blondin, & Pollock (1992), which is the ratio of the postshock cooling timescale to the flow time out of

the system. Hydrodynamical models have indeed confirmed that the postshock gas cools rapidly when $\chi \sim 1.0$.

To evaluate χ we need to determine the pre-shock velocity. χ is highly dependent on this value ($\propto v^4$) so small changes in v make a big change in χ. Using the approximation to the velocity law of St.-Louis et al. (2005),

$$v = v_0 + (v_\infty - v_0) * (1 - R_*/r)^\beta \qquad (1)$$

with $v_0 = 0.16 v_\infty$ and $\beta = 2.5$.

With such a velocity profile the wind accelerates so slowly that the post-shock gas (from both stars) is always highly radiative, and the Cantó et al. (1996) prescription used in Figures 24 and 25 is appropriate. However, if the wind(s) accelerate quicker (e.g. $\beta=1$) then there is a chance that, for example, *star B*'s shocked wind is adiabatic near apastron (but strongly cooling at periastron).

The fact that the X-ray emission is apparently harder near phase 0.36 (Nazé et al. 2007) is very suggestive that the maximum pre-shock velocity increases as the stars separate, although it is by no means certain that the winds between the stars bear much relation to the winds from single stars. Indeed, indications exist that at least *star A*'s wind velocity structure facing the companion differs from that of its opposite hemisphere (Koenigsberger et al. 2006).

Unfortunately there have been very few hydrodynamic calculations of the wind interaction in short period systems like HD 5980 where the acceleration of the winds is taken into account (Iota Ori, Pittard 1998; Sand 1, St-Louis et al. 2005). Antokhin, Owocki, & Brown (2004) took a slightly different approach which enabled them to calculate the X-ray emission, but the wind needed to be specified by a beta velocity law and was not calculated self-consistently with inhibition and braking, in the way that the other hydro models noted were.

If both winds rapidly cool after being shocked, the postshock region collapses into a dense sheet and the shocks are coincident with the contact discontinuity. It is worth noting that in this case one expects very strong instabilities in the WWI region (specifically the non-linear thin-shell instability — see Stevens et al. 1992), which means that the position of the contact discontinuity from the Cantó et al. (1996) model should be viewed only in a time-averaged sense. This is of course a possible cause of the short-timescale fluctuations that are mentioned in § 7).

Wind clumping is an additional factor that is absent from the simplified view of WWI regions.

Pittard (2007) presents simulation of the effects of clumps in binary systems with adiabatic colliding winds. Although the clumps are likely destroyed quite rapidly in such systems, they create a broader distribution of temperatures within the WWI at any given off-axis distance. This is because the inter-clump material is heated to higher than average temperatures, while the clumps are initially heated to significantly lower temperatures (the shocks driven into them are slower) — the temperature within shocked clumps is lower than the temperature obtained from the collision of smooth winds by a factor equal to the density contrast of the clump to interclump material. If most of the wind mass is within the clumps this should have observable consequences. The shocked material within the clumps is then heated further by additional weaker shocks and mixing within the WWI. In systems where the wind parameters are such that a WWI formed by smooth winds is not far from being radiative, the presence of higher densities within clumps may be enough for cooling to become important (see Walder & Folini 2002).

9. CONCLUSIONS

In this paper we present results from spectroscopic and photometric observations of HD 5980 obtained in 1999 and 2003–2005. We first analyze the line-profile variability in the 2005 spectra, concluding that in lines that are formed in the dense, inner wind regions, line-profile-variability may be interpreted mostly in terms of the presence of two emission components, the first belonging to *star A* (the eruptor) and the second associated with *star B* (the companion). Assuming that the emission-line profiles can be effectively separated with a two-function fit, we find that the centroids of the two functions are consistent with the orbital motion of the two stars, leading to a new estimate of the masses, $M_A \sim 58$–79 $M_\odot$ and $M_B \sim 51$–67 $M_\odot$. These values are significantly larger than previously derived (Niemela et al. 1997), but still imply that the stars must have lost considerable amounts of mass before reaching their current evolutionary state, given their location on the HRD near 120 $M_\odot$ ZAMS evolutionary tracks (Koenigsberger 2004). The mechanisms by which such large amounts of mass may have been stripped require detailed examination. In addition, it would be very interesting to get more theoretical insight into their current internal stellar structure and hence, to be able to establish their current evolutionary state. As pointed out by Koenigsberger et al. (1998b), if *star B* is a *bona fide* WNE rem-

nant[18] of the originally more massive member of the binary, its interior may have already reached a very advanced stage of evolution and, thus, it may be nearing the supernova stage. On the other hand, the significantly larger mass that we have now derived for *star B* ($M_\mathrm{B} \sim$56–67 $M_\odot$ *vs.* $\sim$28 $M_\odot$ as believed previously) suggests that it may not yet have reached the core He burning evolutionary phase. Since *star B* is believed to be the source of the highly He-enriched WR-spectrum observed in the 1970's (BMN82), the implications for stellar evolution theory of such a massive, He-rich object are potentially very interesting.

Line strengths in the 2005 spectra are significantly weaker than those observed in 1999, consistent with a similar decreasing trend observed in UV lines, and suggesting that the eruptor is reverting to a more quiescent state. The question of whether another activity cycle will start in the near future is an important one, since the timescale for the eruptive events provides an estimate of the total amount of mass that may be lost through this mechanism. In addition, the activity timescale provides a clue to understanding the underlying mechanism responsible for the instability. Continued observations are required to determine the long-term variability pattern.

Visual photometric observations in 2005 provide a light curve covering the entire orbital cycle, as well as a detailed description of the system's brightness variations during selected orbital phases. In particular, relatively large-amplitude ($\sim$0.035 mag) fluctuations appear around secondary minimum, when *star B*, the non-erupting star, is "in front". Continued systematic observational monitoring around this orbital phase would be very valuable because of the strong and rapid variations observed in visual photometry, polarimetry and UV P Cygni line profiles. In addition, the X-ray appears to be greater here than around the opposite eclipse.

The temporal behavior of the P Cygni absorption components of the He I lines is qualitatively consistent with the presence of a denser wind structure folding around *star B* which we associate with the WWI region. However, the observed speeds are not consistent with the simple models. In particular, the flow speeds are significantly larger than predicted in the radiative shock limit and thus suggest that at least one of the shocks is adiabatic. It is interesting to note that the hemisphere of *star A* that faces the companion is predicted to be particularly active due to tidal interaction effects (Koenigsberger & Moreno 2007), raising the question of how this activity may affect the structure of the WWI region.

The photospheric absorption lines remain stationary over the 19-day orbital cycle. However, we find a systematic shift of $\sim$20 km s^{-1} in their radial velocities observed in 1999 with respect to those observed in 2005. This is consistent with the conclusion of Schweickhardt (2000) that *star C*, the third source in the combined HD 5980 spectrum, is itself a binary system, with $P_\mathrm{starC} \sim$96 days. It is unclear, however, whether the *star C* system is gravitationally bound to the *star A*+*star B* pair with a much longer orbital period. It is a curious fact that the *star C* orbital period is nearly a factor of 5 longer than the orbital period in the *star A*+ *star B* pair, which may indicate that the two systems are physically bound. If this were the case, then the eruptive behavior in HD 5980 could be linked to the gravitational perturbations produced during periastron passages. In this case the orbital period of the *star C* system around the *star A*+ *star B* system would be >25 years, since only one large eruption has been seen over the $\sim$40 years that the system has been studied.

In Table 7 we list the SWOPE and SMARTS photometry averages for each day of observation. The data presented in this paper will be made publicly available (please contact CF or GK).

---

[18]That is, the bare He- or C-burning core of a massive progenitor that has been stripped of its outer layers, as opposed to a massive star in an earlier evolutionary stage undergoing strong wind mass-loss.

TABLE 7

AVERAGE PHOTOMETRIC VISUAL MAGNITUDES: SWOPE AND SMARTS

$< MJD >$	$< phase >$	Num.	$< m_v >$	s.d.	$< MJD >$	$< phase >$	Num.	$< m_v >$	s.d.
52838.379	0.464	16	11.143	0.017	53680.269	0.164	2	11.100	0.002
52839.362	0.515	9	11.154	0.046	53682.075	0.257	4	11.136	0.022
52840.324	0.565	12	11.123	0.019	53683.264	0.319	2	11.195	0.011
52857.303	0.446	18	11.145	0.012	53685.105	0.415	2	11.186	0.001
52858.273	0.497	3	11.122	0.010	53688.131	0.572	2	11.145	0.001
52859.257	0.548	5	11.086	0.018	53689.107	0.622	2	11.133	0.000
52860.244	0.599	1	11.142	$\cdots$	53691.197	0.731	1	11.225	$\cdots$
52972.072	0.404	15	11.185	0.006	53692.077	0.777	2	11.159	0.001
52973.061	0.455	8	11.110	0.008	53694.082	0.881	2	11.189	0.001
52974.059	0.507	16	11.076	0.012	53695.082	0.933	2	11.168	0.008
52975.056	0.559	4	11.090	0.005	53698.036	0.086	2	11.082	0.011
52991.107	0.392	18	11.236	0.018	53700.083	0.192	2	11.087	0.001
52992.063	0.441	19	11.114	0.011	53701.047	0.242	2	11.120	0.002
52992.844	0.482	2	11.073	0.001	53703.075	0.347	2	11.326	0.002
52993.905	0.537	2	11.038	0.008	53704.072	0.399	2	11.255	0.004
53008.062	0.272	7	11.101	0.013	53706.066	0.503	2	11.109	0.017
53009.067	0.324	1	11.170	$\cdots$	53707.092	0.556	2	11.120	0.004
53010.034	0.374	4	11.335	0.013	53710.030	0.709	3	11.109	0.013
53011.039	0.426	6	11.180	0.018	53711.043	0.761	2	11.102	0.021
53159.403	0.127	4	11.048	0.010	53712.096	0.816	2	11.086	0.006
53183.377	0.372	4	11.357	0.016	53714.134	0.922	2	11.121	0.001
53210.325	0.771	7	11.117	0.005	53715.171	0.975	2	11.182	0.020
53225.305	0.548	7	11.109	0.010	53716.027	0.020	2	11.309	0.004
53226.258	0.598	11	11.128	0.011	53719.040	0.176	2	11.110	0.001
53227.387	0.656	6	11.154	0.012	53720.049	0.229	2	11.171	0.001
53228.295	0.703	6	11.128	0.010	53722.022	0.331	2	11.259	0.011
53229.240	0.752	7	11.099	0.016	53724.045	0.436	2	11.160	0.011
53230.228	0.804	8	11.135	0.011	53725.024	0.487	2	11.115	0.023
53247.271	0.688	7	11.153	0.015	53727.029	0.591	2	11.149	0.000
53254.290	0.053	20	11.205	0.013	53752.092	0.892	2	11.142	0.005
53288.193	0.812	26	11.137	0.015	53756.059	0.098	2	11.105	0.001
53591.385	0.550	2	11.119	0.003	53757.027	0.148	2	11.108	0.008
53592.405	0.603	2	11.114	0.003	53758.025	0.200	4	11.135	0.019
53593.400	0.655	1	11.120	$\cdots$	53759.027	0.252	3	11.138	0.035
53596.401	0.810	5	11.122	0.007	53958.306	0.596	1	11.115	$\cdots$
53597.378	0.861	1	11.128	$\cdots$	53960.339	0.701	2	11.120	0.004
53599.223	0.957	2	11.149	0.041	53965.295	0.958	2	11.188	0.002
53600.401	0.018	2	11.325	0.006	53966.310	0.011	2	11.400	0.001
53602.355	0.119	2	11.084	0.005	53968.322	0.116	2	11.143	0.001
53608.313	0.429	2	11.189	0.004	53970.319	0.219	2	11.151	0.003
53615.078	0.780	1	11.158	$\cdots$	53976.356	0.533	2	11.169	0.009
53617.281	0.894	2	11.134	0.006	53983.365	0.896	9	11.183	0.011
53618.199	0.942	3	11.138	0.016	53987.332	0.102	2	11.155	0.001
53619.232	0.995	1	11.347	$\cdots$	53989.342	0.207	2	11.168	0.006
53620.238	0.048	1	11.174	$\cdots$	53991.336	0.310	3	11.168	0.023
53621.379	0.107	2	11.091	0.006	53993.339	0.414	3	11.244	0.008
53622.366	0.158	2	11.069	0.006	53995.325	0.517	2	11.186	0.004
53624.244	0.256	2	11.104	0.008	53998.274	0.670	2	11.126	0.008
53625.326	0.312	2	11.191	0.011	53999.263	0.722	2	11.177	0.021
53628.267	0.464	2	11.142	0.013	54004.245	0.980	2	11.239	0.002
53631.317	0.623	2	11.146	0.004	54007.391	0.143	2	11.091	0.008
53632.323	0.675	2	11.145	0.006	54009.379	0.247	2	11.116	0.014
53634.303	0.778	2	11.126	0.012	54011.350	0.349	2	11.316	0.003
53638.265	0.983	2	11.274	0.008	54013.302	0.450	2	11.177	0.039
53640.255	0.087	2	11.137	0.004	54017.288	0.657	2	11.120	0.007
53642.245	0.190	2	11.107	0.011	54051.014	0.408	2	11.217	0.025
53643.233	0.241	2	11.141	0.014	54052.012	0.460	2	11.155	0.011
53646.201	0.395	2	11.288	0.010	54053.041	0.513	2	11.140	0.012
53650.388	0.613	2	11.181	0.008	54054.033	0.564	2	11.106	0.006
53651.352	0.663	1	11.154	$\cdots$	54056.247	0.679	1	11.124	$\cdots$
53652.397	0.717	2	11.185	0.003	54057.223	0.730	2	11.083	0.000
53655.185	0.862	2	11.101	0.026	54059.177	0.832	2	11.084	0.001
53657.186	0.966	2	11.175	0.018	54061.123	0.933	2	11.122	0.008
53658.132	0.015	4	11.318	0.016	54062.195	0.988	1	11.262	$\cdots$
53660.178	0.121	4	11.070	0.003	54066.001	0.186	4	11.085	0.001
53663.209	0.278	2	11.121	0.001	54068.153	0.297	2	11.130	0.007
53664.219	0.331	2	11.205	0.004	54070.125	0.400	4	11.224	0.015
53665.227	0.383	2	11.329	0.004	54074.173	0.610	2	11.124	0.001
53666.232	0.435	2	11.144	0.003	54080.161	0.921	2	11.148	0.001
53669.062	0.582	4	11.104	0.006	54082.233	0.028	2	11.275	0.004
53670.051	0.633	2	11.121	0.007	54084.189	0.130	2	11.120	0.001
53672.047	0.737	1	11.099	$\cdots$	54086.101	0.229	2	11.151	0.019
53673.020	0.787	3	11.095	0.021	54088.193	0.338	2	11.274	0.004
53675.047	0.893	2	11.139	0.002	54089.195	0.390	2	11.315	0.002
53676.180	0.951	4	11.158	0.006	54090.200	0.442	2	11.156	0.001
53677.196	0.004	2	11.349	0.010	54092.199	0.546	1	11.150	$\cdots$
53679.157	0.106	2	11.150	0.007					

REFERENCES

Antokhin, I. I., Owocki, S. P., & Brown, J. C. 2004, ApJ, 611, 434

Azzopardi, M., & Vigneau, J. 1975, A&AS, 22, 285

Barbá, R. H., Niemela, V. S., Baume, G., & Vázquez, R. A. 1995, ApJ, 446, L23

Barbá, R., Niemela, V. S., & Morrell, N. 1997, in ASP Conf. Ser. 120, Luminous Blue Variables: Massive Stars in transition, ed. A. Nota & H. Lamers (San Francisco: ASP), 238

Barbá, R. H., et al. 1996, RevMexAA (SC), 5, 85

Bateson, F. M., & Jones, A. 1993, R. Astron. Soc. New Zealand Publ. Variable Stars, 19, 50

Breysacher, J., & François, P. 2000, A&A, 361, 231

Breysacher, J., & Perrier, C. 1980, A&A, 90, 207 (BP80)
_____. 1991, in IAU Symp. 143, Wolf Rayet Stars and Interrelations with other Massive Stars in Galaxies, ed. K. van der Hucht & B. Hidayat (Dordrecht: Kluwer), 229 (BP91)

Breysacher, J., Moffat, A. F. J., & Niemela, V. 1982, ApJ, 257, 116 (BMN82)

Breysacher, J., & Westerlund, B. E. 1978, A&A, 67, 261

Cantó, J., Wilkin, F., & Raga, A. 1996, ApJ, 469, 729

Charbonneau, P. 1995, ApJS, 101, 309

De Marco, O. 2002, in ASP Conf. Ser. 260, Interacting Winds from Massive Stars, ed. A. F. J. Moffat & N. St.-Louis (San Francisco: ASP), 517

Demers, H., Moffat, A. F. J, & Marchenko, S. V. 2002, in ASP Conf. Ser. 260, Interacting Winds from Massive Stars, ed. A. F. J. Moffat & N. St.-Louis (San Francisco: ASP), 563

Drissen, L., Crowther, P. A., Smith, L. J., Robert, C., Roy, J.-R., & Hillier, D. J. 2001, ApJ, 545, 484

Everett, M. E., & Howell, S. B. 2001, PASP, 113, 1428

Foellmi, C., Moffat, A. F. J., & Guerrero, M. A. 2003, MNRAS, 338, 1025

Georgiev, L., & Koenigsberger, G. 2004, in IAU Symp. 215, Stellar Rotation, ed. A. Maeder & P. Eenens (San Francisco: ASP), 111

Hoffmann, M., Stift, M. J., & Moffat, A. F. J. 1978, PASP, 90, 101

Kaufer, A., Schmid, H. M., Schweickhardt, J., & Tubbesing, S. 2002, in ASP Conf. Ser. 260, Interacting Winds from Massive Stars, ed. A. F. J. Moffat & N. St.-Louis (San Francisco: ASP), 489

Koenigsberger, G. 2004, RevMexAA, 40, 107

Koenigsberger, G., Auer, L. H., Georgiev, L., & Guinan, E. 1998a, ApJ, 496, 934

Koenigsberger, G., Fullerton, A., Massa, D., & Auer, L. 2006, AJ, 132, 1527

Koenigsberger, G., Guinan, E. Auer, L. H., & Georgiev, L. 1995, ApJ, 452, 107L

Koenigsberger, G., Kurucz, R. L., & Georgiev, L. 2002, ApJ, 581, 598

Koenigsberger, G., & Moreno, E. 2007, RevMexAA (SC), in press (arXiv: 0705.1938v1)

Koenigsberger, G., Peña, M., Schmutz, W., & Ayala, S. 1998b, ApJ, 499, 889

Koenigsberger, G., et al. 2000, ApJ, 542, 428

Koenigsberger, G., et al. 2001, AJ, 121, 267

Marchenko, S. V., Moffat, A. F. J., Eenens, P. R. J., Cardona, O., Echevarría, J., & Hervieux, Y. 1997, ApJ, 485, 826

Marchenko, S. V., Moffat, A. F. J., & Koenigsberger, G. 1994, ApJ, 422, 810

Massey, P., Parker, J. W., & Garmany, C. D. 1989, AJ, 98, 1305

Moffat, A. F. J., et al. 1998, ApJ, 497, 896

Nazé, Y., Corcoran, M. F., Koenigsberger, G., & Moffat, A. F. J. 2007, ApJ, 658, L25

Nielsen, K. E., Corcoran, M. F., Gull, T. R., Hillier, D. J., Hamaguchi, K., Ivarsson, S., & Lindler, D. J. 2007, ApJ, 660, 669

Niemela, V. S. 1988, in ASP Conf. Ser. 1, Progress and Opportunities in Southern Hemisphere Optical Astronomy. The CTIO 25th Anniversary Symposium, ed. V. M. Blanco & M. M. Phillips (San Francisco: ASP), 381

Niemela, V. S., Barbá, R. H., Morrell, N. I., & Corti, M. 1997, in ASP Conf Ser. 120, Luminous Blue Variables: Massive Stars in Transition, ed. A. Nota & H. Lamers (San Francisco: ASP), 222

Pittard, J. M. 1998, MNRAS, 300, 479
_____. 2007, ApJ, 660, L141

Schweickhardt, J. 2000, PhD Thesis, Ruprecht-Karls-Universität, Heidelberg, Germany

Sterken, C., & Breysacher, J. 1997, A&A, 328, 269

Stevens, I. R., Blondin, J. M., & Pollock, A. M. T. 1992, ApJ, 386, 265

St.-Louis, N., Moffat, A. F. J., Marchenko, S. V., & Pittard, J. M. 2005, ApJ, 628, 953

Villar-Sbaffi, A., Moffat, A. F. J., & St.-Louis, N. 2003, ApJ, 590, 483

Walborn, N. R. 1997, ApJ, 215, 53

Walder, R., & Folini, D. 2002, in ASP Conf. Ser. 260, Interacting Winds from Massive Stars, ed. A. F. J. Moffat & N. St.-Louis (San Francisco: ASP), 595

M. Corcoran: CRESST and X-ray Astrophysics Laboratory NASA/GSFC, Greenbelt, MD 20771, USA and Universities Space Research Association, 10211 Wincopin Circle, Suite 500 Columbia, MD 21044, USA (Michael.F.Corcoran.1@gsfc.nasa.gov).

T. H. Dall: Gemini Observatory, 670 N. A'ohoku Pl., Hilo, HI 96720, USA (tdall@gemini.edu).

C. Foellmi: Laboratoire d'AstrOphysique de Grenoble, 414 Rue de la Piscine, Domaine Universitaire, 38400 Saint-Martin d'Hères, France (cedric.foellmi@obs.ujf-grenoble.fr).

A. Fullerton: Space Telescope Science Institute, 3700 San Martin Drive, Baltimore, MD 21218, USA (fullerton@stsci.edu).

L. Georgiev: Instituto de Astronomía, Universidad Nacional Autónoma de México, Apdo. Postal 70-264, 04510 México, D. F., Mexico (georgiev@astroscu.unam.mx).

A. Kaufer: European Southern Observatory, Alonso de Cordova 3107, Casilla 19001, Santiago 19, Chile (akaufer@eso.org).

G. Koenigsberger and O. Toledano: Instituto de Ciencias Físicas, Universidad Nacional Autónoma de México, Av. Universidad s/n, Col. Chamilpa, Cuernavaca, Morelos, 62210, Mexico (gloria@fis.unam.mx, oswaldo-toledano@hotmail.com).

S. V. Marchenko: Department of Physics and Astronomy, Western Kentucky University, 1906 College Heights Blvd #11001, Bowling Green, KY 42101-1101, USA (sergey@astro.wku.edu).

D. Massa: NASA/GSFC, Mailstop 665.0, Greenbelt, MD 20771, USA (massa@taotaomona.gsfc.nasa.gov).

P. Massey: Lowell Observatory, 1400 W Mars Hill Road, Flagstaff, AZ, 86001, USA (Phil.Massey@lowell.edu).

A. F. J. Moffat and N. St.-Louis: Département de Physique, Université de Montréal, C.P. 6128, Succ. Centre-Ville, Montréal, QuebecC, H3C 3J7, and Observatoire du Mont Mégamtic, Canada (moffat, st-louis@astro.umontreal.ca).

N. Morrell: Las Campanas Observatory, Carnegie Observatories, Casilla 601, La Serena, Chile (nidia@lcoeps1.lco.cl; nidia@fcaglp.unlp.edu.ar).

Y. Nazé: FNRS and Institut d'Astrophysique et de Géophysique, Université de Liège, Allée du 6 Août 17, Bat B5C, B4000-Liège, Belgium (naze@astro.ulg.ac.be).

J. Pittard: School of Physics and Astronomy, University of Leeds, Leeds, UK (jmp@ast.leeds.ac.uk).

A. M. T. Pollock: European Space Agency, XMM-Newton SOC, European Space Astronomy Centre, Apdo. 78, 28691 Villanueva de la Cañada, Madrid, Spain (Andy.Pollock@sciops.esa.int).